

A Generalized spatiotemporally ~~-decoupled~~ separated framework for reconstructing the source of ~~non-constant~~ atmospheric radionuclide releases

Yuhan Xu¹, Sheng Fang^{1,*}, Xinwen Dong¹, Shuhan Zhuang¹

¹Institute of Nuclear and New Energy Technology, Collaborative Innovation Centre of Advanced Nuclear Energy Technology, Key Laboratory of Advanced Reactor Engineering and Safety of Ministry of Education, Tsinghua University, Beijing 100084, China

*Correspondence to: Sheng Fang (fangsheng@tsinghua.edu.cn)

Abstract. Determining the source location and release rate are critical tasks in assessing the environmental consequences of atmospheric radionuclide releases, but remain challenging because of the huge multi-dimensional solution space. We propose a generalized spatiotemporally separated spatiotemporally decoupled two-step framework that reduces to reduce the dimension of the solution space in each step and improves the source reconstruction accuracy, which is applicable to non-constant releases. The separation decoupling process applies is conducted by applying a temporal sliding-window average filter to the observations, thereby reducing the influence of temporal variations in the release rate on the observations and ensuring that the features of the filtered data are dominated by the source location. A machine learning model is trained to link these features to the source location, enabling independent source location estimations source localization. Then theThe release rate is then determined using projected alternating minimization with the L1-norm and total variation regularization algorithm. This method is validated against the local-scale SCK-CEN ⁴¹Ar field experiment and the first release of the continental-scale European Tracer Experiment, for which the lowest relative source location errors are 0.60% and 0.20%, respectively. This presents higher accuracy and a smaller uncertainty range than the correlation-based and Bayesian methods in estimating the source location. The temporal variations in release rates are accurately reconstructed, and the mean relative errors of the total release are 65.09% and 72.14% lower than the Bayesian method for the SCK-CEN experiment and European Tracer Experiment, respectively. A sensitivity study demonstrates the robustness of the proposed method to different hyperparameters. With an appropriate site layout, low error levels can be achieved from only a single observation site or under meteorological errors. Validation using SCK-CEN ⁴¹Ar experimental data demonstrates that the localization error is less than 1%, and the temporal variations, peak release rate, and total release are reconstructed accurately. The proposed method exhibits higher accuracy and a smaller uncertainty range than the correlation-based and Bayesian methods. Furthermore, it achieves stable performance with different hyperparameters and produces low error levels even with only a single observation site.

29 1. Introduction

30 Atmospheric radionuclide release is a major environmental concern of the nuclear industry, including nuclear energy and its
31 heat applications, isotope production, and the post-processing of radioactive waste. ~~These Such~~ releases ~~have been observed~~
32 ~~in~~ ~~occurred after~~ the Chernobyl nuclear accident (Anspaugh et al., 1988); and the Fukushima nuclear explosion (Katata et al.,
33 2012), with partially -known source information, i.e. the location. Recently, there have been several atmospheric radionuclide
34 leaks from unknown sources, such as the 2017 ¹⁰⁶Ru leakage (Masson et al., 2019) and the 2020 ^{134/137}Cs detection in northern
35 Europe (Ingremeau and Saunier, 2022), which have raised global concerns regarding the subsequent hazard to public health.
36 Identification of source information in these events is critical for the safe operation of nuclear facilities, consequence
37 assessment, and emergency response.

38 During these events, source ~~information could not~~ ~~data often cannot~~ be directly measured or determined because of the lack
39 of information on the source of the leak. Instead, source information ~~could~~ can only be reconstructed through inversion methods,
40 ~~that identified~~ which identify the optimal solution by comparing the environmental observations with atmospheric dispersion
41 simulations using different estimates of the source location and release rate. Such reconstructions s simultaneously ~~identifies~~
42 ~~identify~~ the source location and release rate because the observations are intuitively determined by both parameters. In this
43 case, the reconstruction searches for ~~the a~~ solution over a ~~tremendous large~~ multi-dimensional space, where the dimension is
44 the sum of the number of space coordinates and the length of the estimated release window. Therefore, the inversion is weakly
45 constrained and can become ill-posed in the case of spatiotemporally limited observations and uncertainties in the atmospheric
46 dispersion models. Unfortunately, this is quite often the case for atmospheric radionuclide releases.

47 To reduce the problem of ill-posedness, most previous studies have attempted to constrain the reconstruction by imposing
48 assumptions on ~~the model–observation discrepancies or release characteristics, a certain feature of the solution, including both~~
49 ~~statistical and deterministic assumptions.~~ ~~Assumptions on model–observation discrepancies~~ ~~Statistical assumptions~~ are widely
50 used in Bayesian methods to simultaneously reconstruct the posterior distributions of spatiotemporal source parameters (De
51 Meutter et al., 2021; Meutter and Hoffman, 2020; Xue et al., 2017a). This assumes that the model–observation discrepancies
52 follow a certain statistical distribution (i.e. the likelihood of Bayesian methods), with the normal (Eslinger and Schrom, 2016;
53 Guo et al., 2009; Keats et al., 2007, 2010; Rajaona et al., 2015; Xue et al., 2017a, b; Yee, 2017; Yee et al., 2008; Zhao et al.,
54 2021) and log-normal (Chow et al., 2008; Dumont Le Brazidec et al., 2020; KIM et al., 2011; Monache et al., 2008; Saunier
55 et al., 2019; Senocak, 2010; Senocak et al., 2008) distributions being two popular choices. Other ~~candidate~~ ~~candidate~~
56 ~~distributions~~ include the t-distribution (with degrees of freedom ranging from 3–10), Cauchy distribution, and log-Cauchy
57 distribution, all of ~~Cauchy, log-Cauchy, and T3-10~~, which ~~were~~ ~~have been~~ compared ~~with~~ ~~against the~~ normal and log-normal
58 distributions in terms of reconstructing the source parameters of the Prairie Grass field experiment (Wang et al., 2017). The
59 results demonstrate that the likelihoods are sensitive to both the dataset and the ~~targeted~~ source parameters. ~~Some~~ ~~Several~~
60 studies have constructed the likelihood based on multiple metrics that measure the model–observation discrepancies in an
61 attempt to better constrain the solution (Lucas et al., 2017; Jensen et al., 2019). More sophisticated methods involve the use of

62 different statistical distributions for the likelihoods of non-detections and detections (De Meutter et al., 2021; Meutter and
63 Hoffman, 2020). Recent studies have suggested the use of log-based distributions and tailored parameterization of the
64 covariance matrix as a means of better quantifying the uncertainties in the reconstruction (Dumont Le Brazidec et al., 2021).
65 These Bayesian methods have been applied to real atmospheric radionuclide releases, such as the 2017 106Ru event, and have
66 provided important insights into the source and release process (Dumont Le Brazidec et al., 2020; Saunier et al., 2019; Dumont
67 Le Brazidec et al., 2021; De Meutter et al., 2021). However, these studies have also revealed that the likelihood in Bayesian
68 methods must be exquisitely designed and parameterized to achieve satisfactory spatiotemporal source reconstruction (Dumont
69 Le Brazidec et al., 2021; Wang et al., 2017). With suboptimal design, the reconstruction may exhibit a bimodal posterior
70 distribution (Meutter and Hoffman, 2020), which remains a challenge for robust applications in different scenarios.

71 Assumptions on the release characteristics aim to reduce the dimension of the solution space to 4 or 5, namely the two source
72 location coordinates, the total release, and the release time (or the release start and end time), i.e. an instantaneous release at
73 one time or constant release over a period (Kovalets et al., 2020, 2018; Efthimiou et al., 2018, 2017; Tomas et al., 2021;
74 Andronopoulos and Kovalets, 2021; Ma et al., 2018). Under these assumptions, the correlation-based method exhibits high
75 accuracy for ideal cases under stationary meteorological conditions, such as synthetic simulation experiments (Ma et al., 2018)
76 and wind tunnel experiments (Kovalets et al., 2018; Efthimiou et al., 2017). However, previous studies have also demonstrated
77 that real-world applications may be much more challenging, (Kovalets et al., 2020; Tomas et al., 2021; Andronopoulos and
78 Kovalets, 2021; Becker et al., 2007) because the release usually exhibits temporal variations and may experience non-
79 stationary meteorological fields. The interaction between the time-varying release characteristics and non-stationary
80 meteorological fields is neglected in the instantaneous-release and constant-release assumptions, leading to inaccurate
81 reconstruction. Deterministic assumptions mainly involve entropy (Krysta and Boequet, 2007; Boequet, 2005b, a) and a
82 constant release rate (Kovalets et al., 2020, 2018; Efthimiou et al., 2018, 2017; Tomas et al., 2021; Andronopoulos and
83 Kovalets, 2021; Ma et al., 2018). Compared with entropy, the constant release assumption is more popular and is embedded
84 in many Bayesian methods (Yee et al., 2008; Eslinger and Schrom, 2016; Meutter and Hoffman, 2020; Zhao et al., 2021; De
85 Meutter et al., 2021), substantially reducing the dimension of the solution space to 5 or 6 (i.e. the two or three source location
86 coordinates, the start and end time of the release, and the total release). Recently, the constant release assumption has been
87 found to enable separate reconstruction of the source location and release rate because the relative spatiotemporal distribution
88 of the simulated atmospheric concentrations is independent of the release rate and is determined by the source location and
89 meteorology (Efthimiou et al., 2017; Kovalets et al., 2018). Because the meteorology can be independently calculated, it is
90 possible to efficiently identify the source location without knowing the specific release rate by simply comparing the
91 correlation coefficients between the observations and simulations using different source locations. The constant release rate is
92 then obtained by calculating a scale factor between the simulation using the identified source location and the observations.
93 This method exhibits high accuracy for constant releases under stationary meteorological conditions, such as synthetic
94 simulation experiments (Ma et al., 2018) and wind tunnel experiments (Kovalets et al., 2018; Efthimiou et al., 2017). However,
95 real releases usually exhibit temporal variations and may experience non-stationary meteorological fields, both of which can

96 lead to noticeable uncertainties in the source localization results of the correlation-based method (Tomas et al., 2021;
97 Andronopoulos and Kovalets, 2021), thus limiting its practical usage. Despite this restriction of the constant release
98 assumption, the correlation-based method does efficiently reduce the solution space for the source localization and release rate
99 estimation, suggesting the potential for reliable source reconstruction.

100 Given the assumption-related reconstruction deviations in complex scenarios, we propose a spatiotemporally separated
101 source reconstruction method that is less dependent on such assumptions. Our approach reduces the complexity of the source
102 reconstruction using the simple fact that the source location is fixed during the atmospheric radionuclide release process. In
103 this case, the spatiotemporal variations of observations are influenced by the time-varying release rate, source location, and
104 meteorology, of which the last variable is generally known. The proposed method reduces the influence of the release rate
105 through a temporal sliding-window average filter, making the filtered observations more sensitive to the source location than
106 to the release rate. After filtering, existing methods based on direct observation–simulation comparisons may be unable to
107 locate the source. In this study, we relax the constant release assumption and propose a more general spatiotemporally
108 decoupled source reconstruction method for non-constant release scenarios. Our approach uses the simple facts that the source
109 location is fixed during the atmospheric radionuclide release process and the peak amplitude of temporal observations is mainly
110 affected by the release rate of a spatially fixed source (Li et al., 2019b). Based on these facts, the proposed method removes
111 the influence of the release rate on the observations through a temporal sliding window average filter, which approximates the
112 constant release case and enables decoupled source localization in the absence of release rate estimation. Because the peak
113 amplitude is reduced, existing methods based on direct observation–simulation comparisons may be unable to localize the
114 source. Thus, the response features of the filtered observations are extracted and mapped to the source location by training a
115 data-driven machine learning model using the extreme gradient boosting (XGBoost) algorithm (Chen and Guestrin, 2016). To
116 fully capture the response features at each observation site, tailored time- and frequency-domain features are designed and
117 optimized using the feature selection technique of XGBoost. Using this optimized model, the source ~~is localized~~ location is
118 estimated based on the filtered observations. Once the source location has been retrieved, the non-constant release rate is
119 determined using the Projected Alternating Minimization with L1-norm and Total variation regularization (PAMILT)
120 algorithm (Fang et al., 2022), which is robust to model uncertainties. The sequential spatiotemporal reconstruction reduces the
121 dimension of the solution space at each step, which helps to improve the accuracy and reliability of the reconstruction.

122 The proposed method is validated using the data from multi-scales field experiments, namely the local-scale SCK-CEN ⁴¹Ar
123 experiment (Rojas-Palma et al., 2004), and the first release of the continental scale European Tracer Experiment (ETEX-1)
124 (Nodop et al., 1998), which traced emissions of Perfluoro-Methyl-Cyclo-Hexane (PMCH). The performance of the proposed
125 method is compared with the correlation-based method (constant release assumption) for in terms of source location
126 estimationsource localization and the Bayesian method (statistical assumption) for in terms of spatiotemporal accuracy. The
127 sensitivity of the source location estimationsource localization to the spatial search range, size of the sliding window, feature
128 type, and number and combination of sites, and meteorological errors is also investigated for the SCK-CEN ⁴¹Ar experiment.

2. Materials and Methods

2.1 Source reconstruction models

For an atmospheric radionuclide release, Eq. (1) relates the observations at each observation site to the source parameters:

$$\boldsymbol{\mu} = \mathbf{F}(\mathbf{r}, \mathbf{q}) + \boldsymbol{\varepsilon}, \quad (1)$$

where $\boldsymbol{\mu} = [\mu_1, \mu_2, \dots, \mu_N]^T \in \mathbb{R}^N$ is an observation vector composed of observations at N sequential time steps, the function \mathbf{F} maps the source parameters to the observations, i.e. an atmospheric dispersion model, \mathbf{r} refers to the source location, $\mathbf{q} \in \mathbb{R}^S$ is the temporally varying release rate, and $\boldsymbol{\varepsilon} \in \mathbb{R}^N$ is a vector containing both model and measurement errors.

In most source reconstruction models, \mathbf{F} is simplified to the product of \mathbf{q} and a source-receptor matrix \mathbf{A} that depends on the source location:

$$\boldsymbol{\mu} = \mathbf{A}(\mathbf{r})\mathbf{q} + \boldsymbol{\varepsilon}, \quad (2)$$

where $\mathbf{A}(\mathbf{r}) = [A_1(\mathbf{r}), A_2(\mathbf{r}), \dots, A_N(\mathbf{r})]^T \in \mathbb{R}^{N \times S}$ and each row describes the sensitivity of an observation to the release rate \mathbf{q} given the source location \mathbf{r} .

2.2 Observation filtering for spatiotemporally separated reconstruction ~~Spatiotemporal decoupling~~

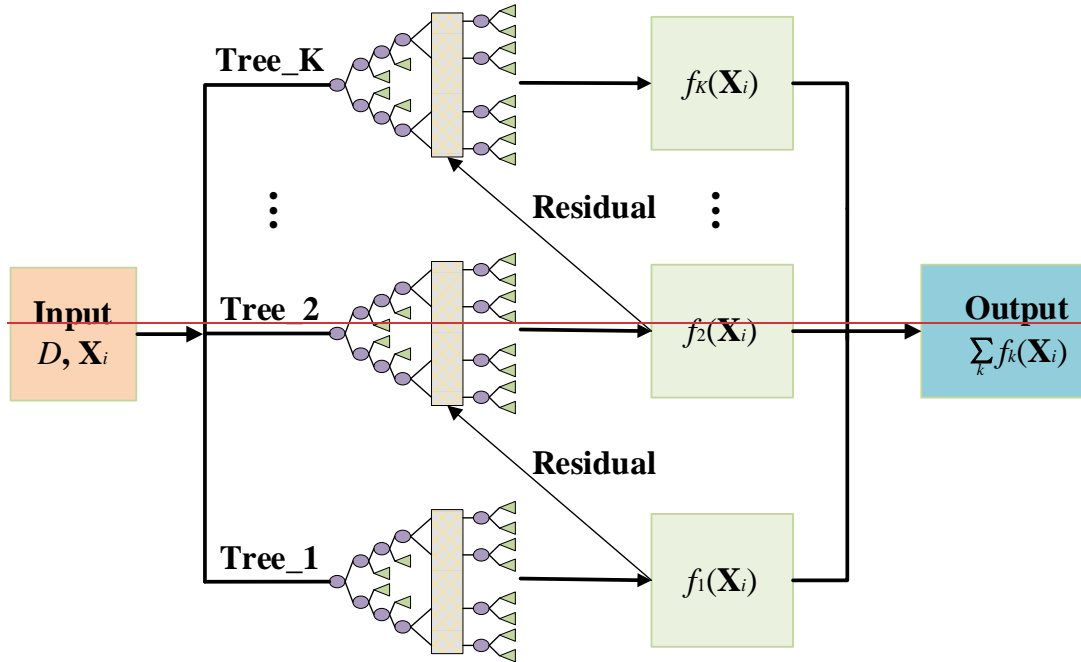
A straightforward way to solve Eq. (2) is to simultaneously retrieve the source location and release rate, ~~which, however,~~ the solution space is huge and difficult to constrain. Several studies have ~~pointed out~~ noted that the source location can be retrieved separately without knowledge of the exact release rate, on the condition that the release rate is constant (Efthimiou et al., 2018; Kovalets et al., 2018; Efthimiou et al., 2017; Ma et al., 2018). The key reason is that, in constant-release cases, the relative spatiotemporal distribution of radionuclides is determined by the meteorological conditions and the relative positions between the source and receptors, and the constant release rate only changes the absolute values. Although the release rate may counteract the influence of the meteorological conditions and relative position at a single observation site, it cannot change the whole spatiotemporal distribution at multiple observation sites. Therefore, by analysing the spatiotemporal distribution of radionuclides at multiple observation sites, it is possible to localize the source without knowing the release rate under the constant-release assumption.

To provide a more general method, we take advantage of the fact that the source location has been fixed during all known atmospheric radionuclide releases, such as the Chernobyl nuclear accident (Anspaugh et al., 1988), ~~the~~ Fukushima nuclear explosion (Katata et al., 2012), and ~~the~~ 2017 ^{106}Ru leakage (Masson et al., 2019). With a fixed source location, the release rate and meteorology jointly determine the temporal variations of the observations (Li et al., 2019b). ~~mainly influences the peak values of the temporal observations at each site, whereas the meteorology determines the timing of the peaks (Li et al., 2019b).~~ The influence of meteorology can be pre-calculated as the source-receptor sensitivities and subsequently stored in matrix $\mathbf{A}(\mathbf{r})$.

184 $\mathbf{r}_i = (x_i, y_i)$ is the location vector. XGBoost typically uses multiple decision trees (Fig. 1) to fit the target, which can be
 185 formulated as:

186
$$\hat{\mathbf{r}}_i = G(\mathbf{X}) = \sum_{k=1}^K f_k(\mathbf{X}_i), f_k \in \mathcal{F}, \quad (5)$$

187 where K is the number of trees, $\mathcal{F} = \{f(x) = \omega_{Q(x)}\} (Q: \mathbb{R}^p \rightarrow M, \omega \in \mathbb{R}^M)$ is the space of the decision trees, and Q
 188 represents the structure of each tree, mapping the feature vector to M leaf nodes. Each f_k corresponds to an independent tree
 189 structure Q with leaf node weights $\omega = (\omega_1, \omega_2, \dots, \omega_M)$. Equation (5) is then used to predict $\hat{\mathbf{r}}_i = (\hat{x}_i, \hat{y}_i)$ for the i -th
 190 sample.



191

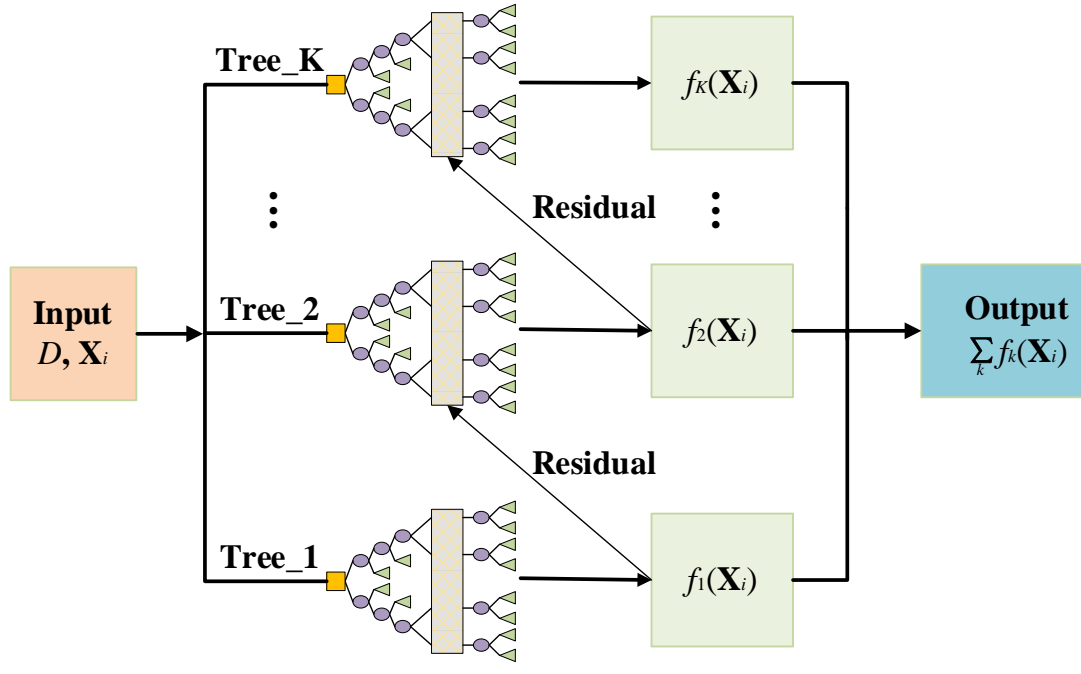


Figure 1. Flowchart of XGBoost for predicting \hat{r}_i based on decision tree model. The yellow squares are the root nodes within each tree, representing the input features in this paper. The purple ellipses denote the child nodes where the model evaluates input features and make decisions to split the data. The green rectangles depict the leaf nodes and refer to the prediction results. The vertical rectangles abstract the internal splitting processes of the trees, indicating decision-making not explicitly detailed in the diagram.

XGBoost trains $G(\mathbf{X})$ in Eq. (5) by continuously fitting the residual error until the following objective function is minimized:

$$Obj^{(t)} = \sum_{i=1}^n \left(\mathbf{r}_i - \left(\hat{\mathbf{r}}_i^{(t-1)} + f_t(\mathbf{X}_i) \right) \right)^2 + \sum_{i=1}^t \Omega(f_i), \quad (6)$$

where t represents the training of the t -th tree and $\Omega(f_i)$ is the regularization term, given by:

$$\Omega(f) = YFM + \frac{1}{2} \lambda \sum_{j=1}^{MF} \omega_j^2, \quad (7)$$

where M is the number of leaf nodes, ω_j is the leaf node weight for the j -th leaf node, and Y, λ are penalty coefficients. The minimization of Eq. (6) provides ~~the a~~ parametric model $G(\mathbf{X})$ that maps the feature ensemble \mathbf{X} extracted from μ_p to the source location \mathbf{r} .

To comprehensively evaluate the influence of the source location, both time- and frequency-domain features (as outlined in Table 1) are considered during the training process and mapped to the source location by $G(\mathbf{X})$. Among the time-domain features, the wave rate quantifies the fluctuations of μ_p over time~~the amplitude of fluctuations in μ_p~~ , while the temporal mean and median values are measures of the central tendency of μ_p ~~(Witte and Witte, 2017).~~represent the central moment of μ_p . ~~Additionally, τ~~ The sample entropy measures the complexity of μ_p , with a lower sample entropy indicating greater self-

209 similarity and less randomness in $\boldsymbol{\mu}_p$. The frequency-domain features are calculated based on the fast Fourier transform (FFT).
 210 The FFT mean is the mean value of the Fourier coefficients for $\boldsymbol{\mu}_p$ and the FFT shape mean describes the shape of the Fourier
 211 coefficients. These quantities are formulated as follows:

$$212 \text{ FFT mean} = \frac{1}{N} \sum_{k=1}^N |\mu_{ik}|, \quad (8)$$

$$213 \text{ FFT shape mean} = \frac{1}{\sum_{k=1}^N |\mu_{ik}|} \sum_{k=1}^N k |\mu_{ik}|, \quad (9)$$

214 where μ_{ik} is the Fourier coefficient and N is the length of $\boldsymbol{\mu}_p$. These features are calculated from the simulated observations at
 215 each site and provided to XGBoost as initial inputs.

216 **Table 1.** Summary of the basic information on the observation series features.

Attribute	Feature	Description
Time domain	Wave rate	Difference between 90-th and 10-th quantile of normalized observation series
	Mean	Temporal mean value of observation series
	Median	Temporal median value of observation series
Frequency domain	Sample entropy	Complexity of observation series
	FFT mean	Amplitude of power spectral density by FFT
	FFT shape mean	Shape of power spectral density by FFT

217 2.4 Release rate estimation

218 Once the source location has been retrieved, many existing methods can be used to inversely estimate the release rate. In this
 219 study, we choose the recently developed PAMILT method (Fang et al., 2022) because it can correct the intrinsic model errors
 220 of the release rate estimation and accurately retrieve the temporal variations in the release rates, reduce the propagation of
 221 localization errors into the release rate estimate.

222 2.5 Numerical implementation

223 2.5.1 Pre-screening of potential source locations

224 To reduce the computational cost and remove low-quality samples, the search range for the source location is pre-screened by
 225 evaluating the correlation coefficients between the observations and atmospheric dispersion model simulations, where the
 226 candidate source locations are randomly sampled in the considered calculation domain. Because the release rate is unknown,
 227 it is assumed to be 1 ~~Bq/h~~ for all simulations. Source locations corresponding to the highest 40% of correlation

228 ~~coefficients~~ These source locations corresponding to correlation coefficients above the 40th percentile are selected as the search
229 range of the subsequent refined ~~source localization~~ source location estimation using XGBoost.

230 2.5.2 Samples for training XGBoost

231 The samples for training $G(\mathbf{X})$ in Eq. (5) are generated based on the simulations described in Sect. 2.5.1, and the source
232 locations of these simulations are within the search range ~~as~~ determined according to Sect. 2.5.1. The simulation data are scaled
233 by a constant factor (the ratio between the median value of all observations and that of the simulations using a unit release
234 rate), which ensures that the simulations and observations have the same order of magnitude. Gaussian noise is added to the
235 simulation data to simulate the statistical fluctuations of ~~radiation-the~~ measurements. ~~Those~~ The simulations between the first
236 and last data points above the noise level are filtered by a temporal sliding-window average filter with a window size of 5,
237 yielding samples for feature extraction as described in Sect. 2.3.

238 2.5.3 Automatic optimization of XGBoost model

239 The XGBoost model for ~~source localization~~ source location estimation is automatically optimized with respect to the
240 hyperparameters and feature selection. Specifically, the Bayesian optimization algorithm is used to optimize the
241 hyperparameters by minimizing the following generalization coefficient (GC) defined under the five-fold cross-validation
242 framework:

$$243 \text{GC} = (1 - \text{MCV})^2 + \text{Var}(R_k^2), \quad (10)$$

$$244 \text{MCV} = \frac{1}{5} \sum_k R_k^2, \quad (11)$$

245 where R_k^2 is the goodness of fit and k is the index of each fold ($k = 1, 2, \dots, 5$). MCV is the mean cross-validation score R_k^2
246 among the five folds and $\text{Var}(R_k^2)$ measures the variance of R_k^2 . This function aims to balance the average and the variance of
247 R_k^2 , thus enhancing the generalization ability of the XGBoost model. In this study, the optimized hyperparameters include
248 *max_depth* (maximum depth of a decision tree), *learning_rate* (step size shrinkage when updating), *n_estimators* (number of
249 decision trees), *min_child_weight* (minimum sum of sample weight of a child node), *subsample* (subsample ratio of the training
250 samples), *colsample_bytree* (subsample ratio of columns when constructing a decision tree), *reg_lambda* (L2 regularization
251 term on weights), and *gamma* (minimum loss reduction required to split the decision tree).

252 The initial input features (Table 1) are optimized through a feature selection step, where MCV serves as the selection
253 criterion. The selection is implemented by recursively removing the feature with the least importance, and reassessing the
254 MCV based on cross-validation (Akhtar et al., 2019). Initially, an XGBoost model is trained with all features, and the
255 importance of each feature is assessed based on its contribution to the model accuracy. The feature with the least importance
256 is removed and the XGBoost model is retrained using the remaining features. The feature importance and MCV are updated
257 accordingly and another feature is removed. This iterative process continues until the optimal number of features is identified.

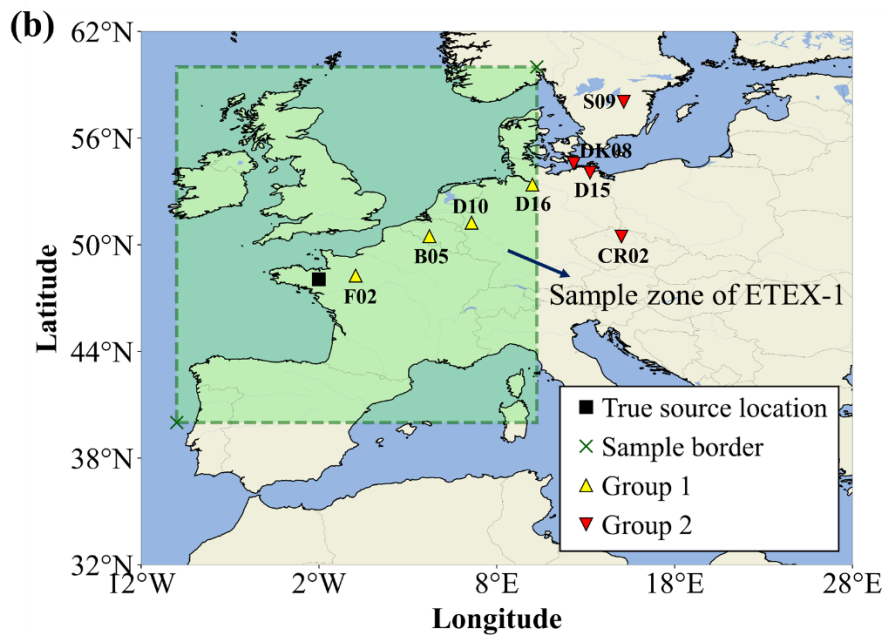
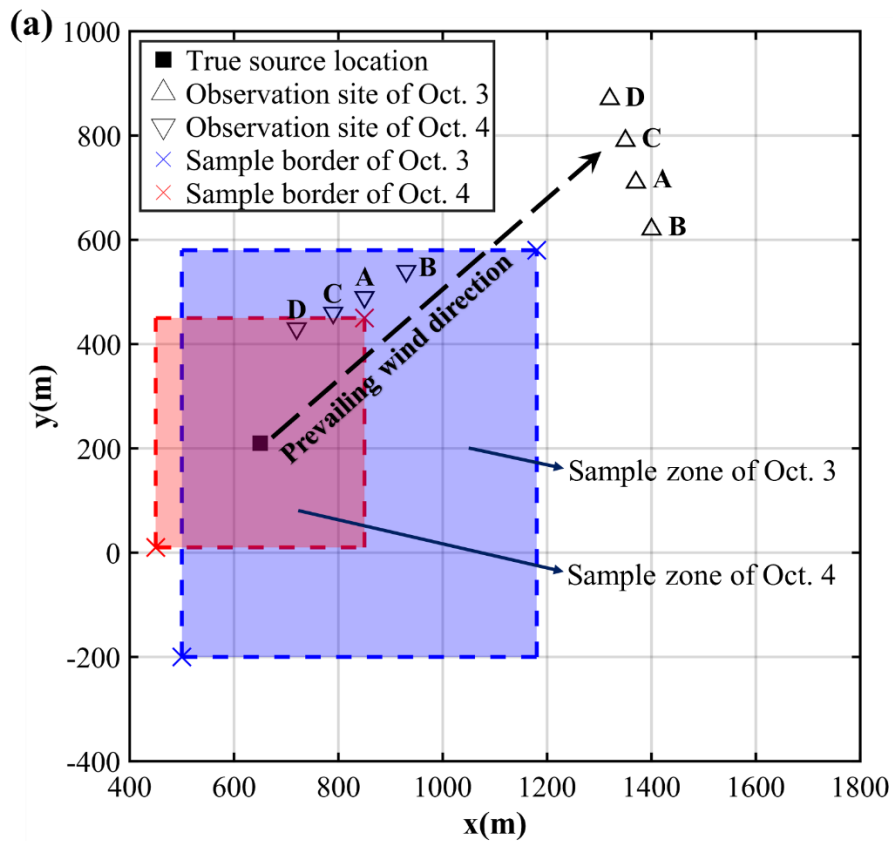
258 ~~corresponding to the highest MCV achieved during the process. by recursive feature elimination with cross-validation (Alkhtar~~
259 ~~et al., 2019), which sorts the features in order of importance and removes the least important features based on the MCV results.~~
260 The overall flowchart of the proposed spatiotemporally ~~decoupled-separated~~ source reconstruction model is shown in Fig. S1.

261 2.6 Validation case

262 2.6.1 ~~SCK-CEN ⁴¹Ar field experiment~~ Field experiments

263 The proposed methodology was validated against the observations of the SCK-CEN ⁴¹Ar ~~and ETEX-1~~ field experiments. ~~The~~
264 ~~SCK-CEN ⁴¹Ar experiment, which~~ was carried out at the BR1 research reactor in Mol, Belgium, in October 2001 as a
265 collaboration between NKS and the Belgian Nuclear Research Centre (SCK-CEN) (Rojas-Palma et al., 2004). The major part
266 of the experiment was conducted on 3–4 October, during which time ⁴¹Ar was emitted from a 60-m stack with a release rate
267 of approximately $1.5 \times 10^{11} \text{ Bq h}^{-1}$ ~~$1.5 \times 10^{11} \text{ Bq/h}$~~ . Meteorological data such as wind speed and direction were provided by
268 the on-site weather mast. For most of the experimental period, the atmospheric stability was neutral, and the wind was blowing
269 from the southwest. As illustrated in Fig. 2(a), the source coordinates were (650 m, 210 m). The 60-s-average ground-level
270 fluence rates were continuously collected by an array of NaI (TI) gamma detectors, with different observation sites used on
271 the two days. To convert the measured fluence rates to gamma dose rates (mSv/h), we used the ⁴¹Ar parameters of a previous
272 study (Li et al., 2019a): $E_\gamma = 1.2938 \text{ MeV}$, $f^n(E_\gamma) = 0.9921$, $\mu_a = 2.05 \times 10^{-3} \text{ m}^{-1}$, and $\omega = 7.3516 \times 10^{-1} \text{ Sv Gy}^{-1}$.
273 More details of these measurements can be found in (Rojas-Palma et al., 2004).

274 The ETEX-1 experiment took place at Monterfil in Brittany, France, on 23 October 1994 (Nodop et al., 1998). During
275 ETEX-1, a total of 340 kg of PMCH was released into the atmosphere on 23 October 1994 at 16:00:00 UTC and 24 October
276 1994 at 03:50:00 UTC. As illustrated in Fig. 2(b), the source coordinates were (-2.0083°E, 48.058°N). A total of 3104 available
277 observations (3-h-averaged concentrations) were collected at 168 ground sites. ETEX-1 has been widely used as a validation
278 scenario for reconstructing atmospheric radionuclide releases (Ulimoen and Klein, 2023; Tomas et al., 2021). The candidate
279 source locations are uniformly sampled from the green shaded zone. We choose two groups of observation sites: the first
280 comprises four sites (i.e. B05, D10, D16, F02) randomly selected from the sites within the sample zone (Group 1, with a total
281 of 92 available observations), and the second involves four sites (i.e. CR02, D15, DK08, S09) randomly selected from the sites
282 beyond the sample zone boundaries (Group 2, with a total of 90 available observations). Compared with the SCK-CEN ⁴¹Ar
283 experiment, the ETEX-1 observations exhibit temporal sparsity, lower temporal resolution, and increased complexity in
284 meteorological conditions.



285

286

Figure 2. Release location and observation sites of two field experiments. (a) SCK-CEN ^{41}Ar experiment. The map was created based on

287 the relative positions of the release source and observation sites (Drews et al., 2002). The coordinates of the sample border are (500 m, -200
288 m) and (1180 m, 580 m) on Oct. 3, and (450 m, 10 m) and (850 m, 450 m) on Oct. 4. This figure was plotted using MATLAB 2016b, rather
289 than created by a map provider; (b) ETEX-1 experiment. The map was created based on the real longitudes and latitudes of the release source
290 and observation sites (Nodop et al., 1998). The coordinates of the sample border are (10°W, 40°N) and (10°E, 60°N). This figure was plotted
291 using the cartopy function of Python, rather than created by a map provider.
292 SCK-CEN ⁴¹Ar experiment. The map was created based on the
293 relative positions of the release source and observation sites, as detailed in (Drews et al., 2002). It was plotted using MATLAB 2016b,
instead of created by a map provider.

294 The 60 s average fluence rates were continuously collected by an array of NaI (TI) gamma detectors, with different observation
295 sites used on the two days. To convert the measured fluence rates to gamma dose rates (mSv/h), we used the ⁴¹Ar parameters
296 of a previous study (Li et al., 2019a): $E_{\gamma} = 1.2938$ MeV, $f^{\pi}(E_{\gamma}) = 0.9921$, $\mu_{a} = 2.05 \times 10^{-3} \text{ m}^{-1}$, and $\omega = 7.3516 \times$
297 10^{-1} Sv/Gy . More details of these measurements can be found in reference (Rojas Palma et al., 2004).

298 **2.6.2 Simulation settings of atmospheric dispersion model**

299 For the SCK-CEN ⁴¹Ar field experiment, The-the Risø Mesoscale PUFF (RIMPUFF) model was employed to simulate the
300 dispersion of radionuclides and ~~to~~ calculate the dose rates at each observation site (Thykier-Nielsen et al., 1999). The
301 simulations used on-site measured meteorological data and the modified Karlsruhe-Jülich diffusion coefficients. The
302 calculation domain measured 1800 m×1800 m and the grid resolution was 10 m×10 m. The release height of ⁴¹Ar was assumed
303 to be 60 m. Other RIMPUFF calculation settings followed those of a previous study (Li et al., 2019a), and have been validated
304 against the observations. To establish the datasets for the XGBoost model, 2000 simulations and 1000 simulations with
305 different source locations were performed~~2000 samples and 1000 samples with different source locations were calculated~~ by
306 RIMPUFF for the experiments on Oct. 3 and Oct. 4, respectively. ~~The-Candidate~~ source locations were randomly sampled
307 from the shaded zones in Fig. 2(a), which were determined according to the positions of the observation sites and the upwind
308 direction. Each simulation, along with its corresponding source location, forms one sample. As described in Sect. 2.5.1,
309 we calculated the correlation coefficient for each sample and preserved the 40% of samples with the highest 40% of correlation
310 coefficients~~samples with correlation coefficients greater than the 40th percentile of all correlation coefficients~~ (i.e. 800 samples
311 for Oct. 3 and 400 samples for Oct. 4). The constant factors mentioned in Sect. 2.5.2 are 1.53×10^{11} ~~1.53×10^{11}~~ and 1.48×10^{11}
312 ~~1.48×10^{11}~~ for Oct. 3 and Oct. 4, respectively.

313 For the ETEX-1 experiment, the FLEXible PARTicle (FLEXPART) model (version 10.4) was applied to simulate the
314 dispersion of PMCH (Pisso et al., 2019). The meteorological data were obtained from the United States National Centers of
315 Environmental Prediction Climate Forecast System Reanalysis, and have a spatial resolution of $0.5^{\circ} \times 0.5^{\circ}$ and time resolution
316 of 6 h. To rapidly establish the relationship between the varying source locations and the observations, 182 backward
317 simulations were performed using FLEXPART with a time interval of 3 h, grid size of $0.25^{\circ} \times 0.25^{\circ}$, and 8 vertical levels (from
318 100–50000 m). Only the lowest model output layer was used for source reconstruction. Candidate source locations were
319 uniformly sampled from the shaded zone in Fig. 2(b), resulting in a total of 6561 source locations. As described in Sect. 2.5.1,
320 2624 candidate source locations were preserved following the pre-screening step. The constant factors mentioned in Sect. 2.5.2
321 are 5.60×10^{12} and 2.86×10^{13} for Group 1 and Group 2, respectively.

322 2.7 Sensitivity study

323 (1) Search range

324 The search range is controlled by the pre-screening threshold, which is the top proportion of the correlation coefficients in
325 the pre-screening step. Specifically, we use source locations corresponding to the highest 20%, 40%, 50%, 60%, 80%, and
326 100% of correlation coefficients to define the search ranges, with a lower proportion indicating a narrower and more focused
327 search area. The source localization is implemented with pre-screening thresholds determined by the 20th, 40th, 50th, 60th,
328 80th, and 100th percentiles of the correlation coefficients in the pre-screening step, where a lower percentile corresponds to a
329 more refined search range.

330 (2) Size of the sliding window

331 Temporal filtering with different sliding-window sizes is applied to ~~decouple-separate~~ the ~~source-localization~~source location
332 estimation from the release rate estimation. In this study, the size of the sliding window ranges from 3 ~~to~~ 10. With these
333 ~~decoupled-filtered~~ data, the XGBoost model is trained using the same pattern for the ~~source-localization~~source location
334 estimation.

335 (3) Feature type

336 The XGBoost model is trained using only time-domain features and only frequency-domain features, ~~respectively,~~ to
337 investigate the influence of these features on the ~~source-localization~~source location estimation. The performance of the time-
338 feature-only and frequency-feature-only models is compared with the all-features result.

339 (4) Number and combination of observation sites

340 The XGBoost model is trained and applied to the ~~source-localization~~source location estimation with different numbers of
341 observation sites, namely a single site, two sites, and three sites. For the two- and three-site cases, the model is trained using
342 different combinations of sites and the source location is estimated accordingly.

343 (5) Meteorological errors

344 Meteorological errors are important uncertainties in source reconstruction, especially the random errors in the wind field
345 (Mekhaimr and Abdel Wahab, 2019). To simulate such uncertainties, a stochastic perturbation of $\pm 10\%$ is introduced to the
346 observed wind speeds in the x and y components, and a ± 1 stability class perturbation is applied to the stability parameters
347 (e.g., from C to B or D). For both days, 50 meteorological groups are generated based on these random perturbations.

348 In all the sensitivity tests, the source location is estimated 50 times with randomly initialized hyperparameters to demonstrate
349 the uncertainty range of the proposed method under different circumstances. The performance of ~~source-localization~~source
350 location estimation is compared quantitatively using the metrics specified in Sect. 2.8.3.

351 2.8 Performance evaluation

352 2.8.1 Observation filtering~~Decoupling~~

353 The feasibility of ~~decoupling-filtering~~ was-is demonstrated using both the synthetic and real observations of the SCK-CEN

354 ⁴¹Ar ~~field experiment~~ and the real observations of the ETEX-1 experiment. ~~The synthetic observations are~~ The former were
 355 generated by a simulation using a synthetic temporally varying release profile with sharp increase, stable, and gradual decrease
 356 phases (as illustrated in Fig. S2), which is typical for an atmospheric radionuclide release (Davoine and Bocquet, 2007).
 357 Because several temporal observations are missing at some observation sites, we only choose observations sampled between
 358 24 October 1994 09:00:00 UTC and 26 October 1994 03:00:00 UTC for the source location estimation. The simulations
 359 corresponding to the synthetic and real observations should first be processed following the procedure described in Sect. 2.5.2.
 360 The ~~decoupling-filtering~~ performance is evaluated by comparing the simulation-observation differences before and after the
 361 ~~decoupling-filtering~~ step. Several statistical metrics can be used to quantify this difference, including the normalized mean
 362 square error (NMSE), Pearson’s correlation coefficient (PCC), and the fraction of predictions within a factor of 2 and 5 of the
 363 observations (FAC 2 and FAC 5, respectively) (Chang and Hanna, 2004).

364 2.8.2 Optimization of the XGBoost model

365 The hyperparameters are optimized with respect to the GC in Eq. (10) and the features are optimized with respect to the MCV
 366 in Eq. (11). Larger values of MCV and smaller values of GC indicate better optimization performance. In addition, the
 367 importance of each feature to the XGBoost training is evaluated with the built-in *feature importance* measure of the XGBoost
 368 model.

369 2.8.3 Source reconstruction

370 The relative errors ~~of in the~~ source ~~localization-location~~ (δ_r) and total release (δ_Q) are calculated to evaluate the source
 371 reconstruction accuracy:

$$372 \delta_r = \frac{|r_{true} - r_{est}|}{L_D} \times 100\% , \quad (12)$$

$$373 \delta_Q = \frac{Q_{true} - Q_{est} + |Q_{true} - Q_{est}|}{Q_{true}} \times 100\% ,$$

374 _____ (13)

375 where r_{true} and Q_{true} refer to the real source location and total release of the ~~SCK-CEN-⁴¹Ar~~ field experiment and r_{est} and
 376 Q_{est} are the estimated location and total release, respectively. L_D represents the range of the source domain, which is the
 377 distance between the lower and upper borders of the sampled zone (Fig. 2). The values of r_{true} , L_D , and Q_{true} are listed in
 378 Table 2, equal to 1034.8 m and 565.7 m on Oct. 3 and Oct. 4, respectively. In addition to the total release, the reconstructed
 379 release rates are also compared with the true ~~value in terms of the~~ temporal release profile.

380 Table 2. Parameter settings of field experiments.

<u>Experiment</u>	<u>Case</u>	<u>Parameters</u>
-------------------	-------------	-------------------

		r_{true}	L_D	Q_{true}
<u>SCK-CEN ⁴¹Ar</u>	<u>Oct. 3</u>	<u>(650 m, 210 m)</u>	<u>1034.8 m</u>	<u>423.10 GBq</u>
	<u>Oct. 4</u>	<u>(650 m, 210 m)</u>	<u>565.7 m</u>	<u>1045.09 GBq</u>
<u>ETEX-1</u>	<u>Group 1</u>	<u>(2.0083°W, 48.058°N)</u>	<u>2620.5 km</u>	<u>340 kg</u>
	<u>Group 2</u>	<u>(2.0083°W, 48.058°N)</u>	<u>2620.5 km</u>	<u>340 kg</u>

381 2.8.4 Comparison with the Bayesian method

382 The proposed method is compared with the popular Bayesian method based on the SCK-CEN ⁴¹Ar and ETEX-1
383 experimentsexperiment, with the same search range used for locating the sourcesource localization in both methods (Fig. 2).
384 The Bayesian method is augmented with an in-loop inversion of the release rate at each iteration step of the Markov chain
385 Monte Carlo sampling. The prior distribution of the Bayesian method is a uniform distribution and the likelihood is a log-
386 Cauchy distribution. More detailed information is presented in Supplementary Note S1.

387 2.8.5 Uncertainty range

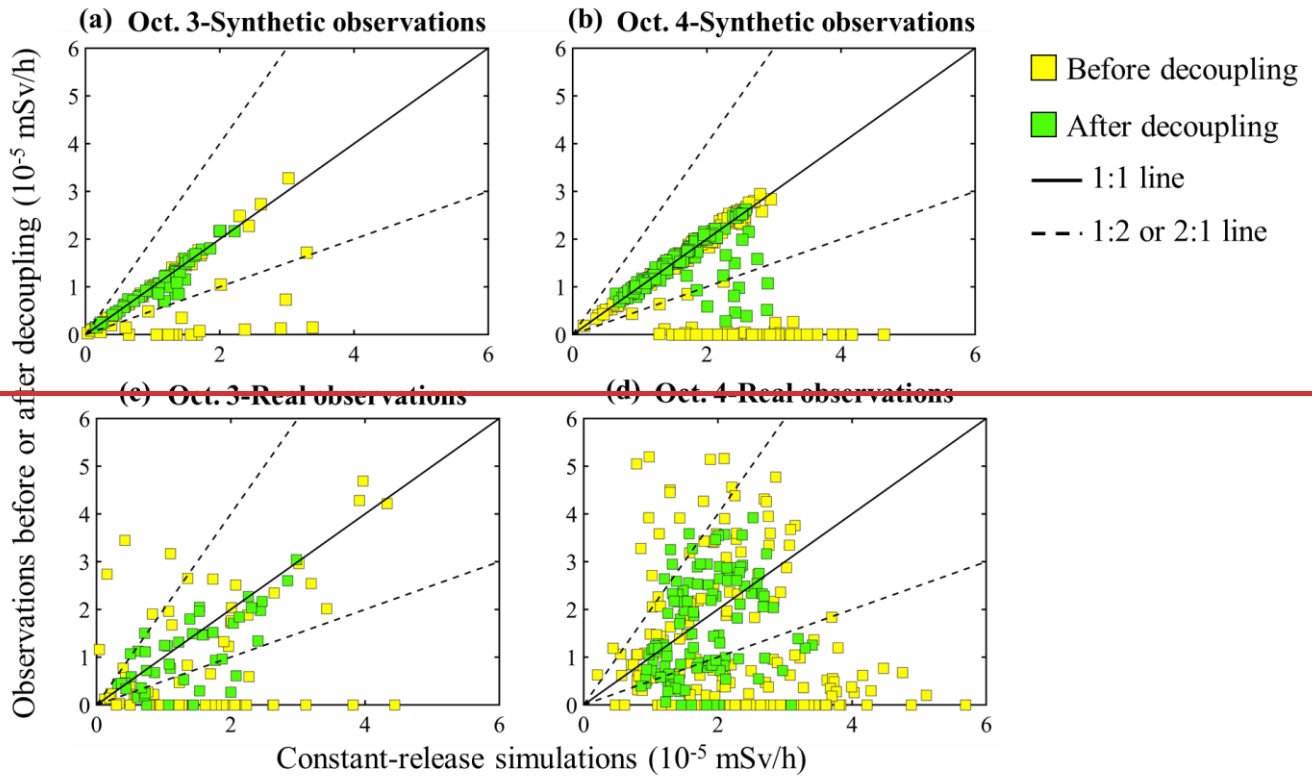
388 The uncertainty ranges are calculated and compared for the correlation-based method, the Bayesian method, and the proposed
389 method. For the correlation-based method, the uncertainty range is calculated using the source locations with the top-50
390 correlation coefficients. For the proposed method, the uncertainty range is calculated from 50 Monte Carlo runs with randomly
391 initialized hyperparameters. The Bayesian method itself provides the uncertainty range directly through the posterior
392 distribution. To be consistentFor consistency with the other two methods, the results with the top-50 frequencies are selected
393 for the comparison.

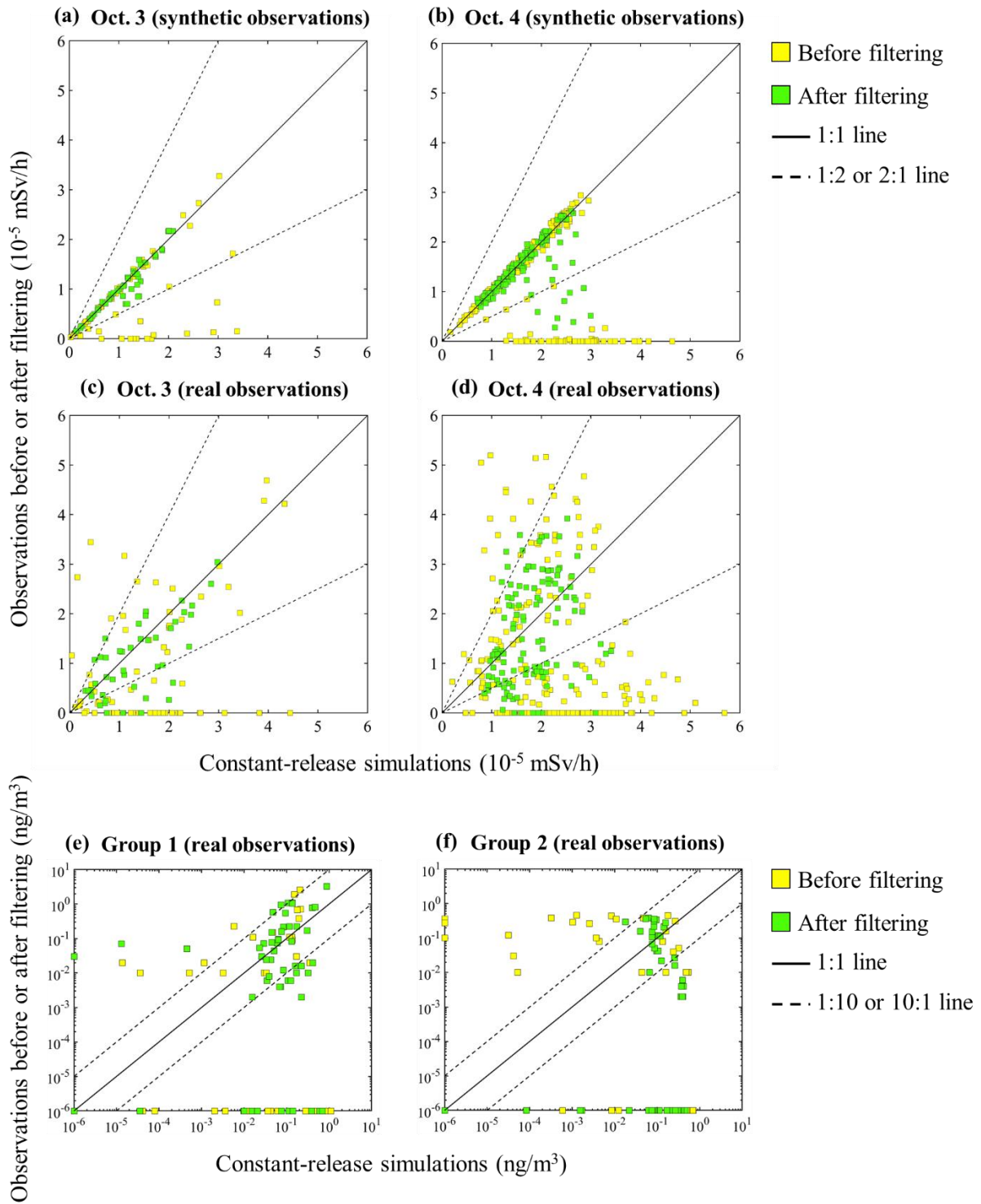
394 3. Results and Discussion

395 3.1 ~~Decoupling-Filtering~~ performance

396 Figure S3 displays the original and filtered observations at different observation sites for both days. The results demonstrate
397 that the peak values have been smoothed out and the long-term trends are preserved to a large degree. Figure 3 compares the
398 ~~decoupling-filtering~~ performance for both the synthetic and real observations, by plottingwhere the constant-release
399 simulations are plotted against the observations before and after ~~decouplingfiltering~~. For the synthetic observations, the
400 ~~decoupled-filtered~~ data are more concentrated along the 1:1 line for both days, and all ~~the decoupledfiltered~~ data fall within
401 the 2-fold lines for Oct. 3. For the real observations, the dots before ~~decoupling-filtering~~ in Fig. 3 have a dispersed distribution
402 for both Oct. 3 and Oct. 4, indicating limited correlations with the simulations. After ~~decouplingfiltering~~, the dots are more
403 concentrated along-towards the 1:1 and 1:2 (2:1) lines for both the SCK-CEN ⁴¹Ar and ETEX-1 experiments. These phenomena

indicate a noticeably increased agreement between the ~~decoupled~~-filtered observations and the constant-release simulations.





406

407

Figure 3. Scatter plots of the original (yellow squares) and decoupled-filtered (green squares) observations versus the constant-release

simulation results. SCK-CEN ⁴¹Ar experiment: (a) Oct. 3 (synthetic observations); (b) Oct. 4 (synthetic observations); (c) Oct. 3 (real observations); (d) Oct. 4 (real observations); ETEX-1 experiment: (e) Group 1 (real observations); (f) Group 2 (real observations). ~~(a) Oct. 3 Synthetic observations; (b) Oct. 4 Synthetic observations; (c) Oct. 3 Real observations; (d) Oct. 4 Real observations.~~

~~Table 2~~ Table 3 quantitatively compares the ~~agreements~~ results presented in Fig. 3. For ~~both the synthetic and real observations~~ each case, all metrics are greatly improved after ~~decoupling filtering~~, especially NMSE and PCC, confirming the better agreement between the ~~decoupled-filtered~~ observations and the constant-release simulations. The improved agreement indicates that the filtering step significantly reduces the influence of temporal variations in release rates across the observations. The ~~decoupling filtering~~ performs better with the synthetic observations than with the real observations. ~~This is~~ because the synthetic observations are free of measurement errors. The filtering process produces a better effect with the SCK-CEN ⁴¹Ar experiment than with the ETEX-1 experiment, owing to the sparser observations in the ETEX-1 experiment (Fig. S3). ~~The improved agreement indicates that the decoupling step significantly reduces the influence of temporal variations in release rates across the real observations.~~

Table 23. Quantitative metrics for the ~~decoupling filtering~~ validation.

<u>Experiment</u>	<u>Case</u>	<u>NMSE</u>	<u>PCC</u>	<u>FAC2</u>	<u>FAC5</u>	
<u>SCK-CEN ⁴¹Ar</u>	<u>Oct. 3 (synthetic observations)</u>	<u>Before filtering</u>	<u>0.6970</u>	<u>0.5315</u>	<u>0.7647</u>	<u>0.8235</u>
		<u>After filtering</u>	<u>0.0239</u>	<u>0.9514</u>	<u>1</u>	<u>1</u>
	<u>Oct. 4 (synthetic observations)</u>	<u>Before filtering</u>	<u>0.9290</u>	<u>-0.0267</u>	<u>0.7292</u>	<u>0.7292</u>
		<u>After filtering</u>	<u>0.0956</u>	<u>0.6179</u>	<u>0.9412</u>	<u>0.9779</u>
	<u>Oct. 3 (real observations)</u>	<u>Before filtering</u>	<u>1.4437</u>	<u>0.3572</u>	<u>0.3824</u>	<u>0.5147</u>
		<u>After filtering</u>	<u>0.2730</u>	<u>0.6976</u>	<u>0.7273</u>	<u>0.8864</u>
		<u>Before filtering</u>	<u>1.9290</u>	<u>-0.2099</u>	<u>0.3073</u>	<u>0.4948</u>
		<u>After filtering</u>	<u>0.3668</u>	<u>0.2802</u>	<u>0.6552</u>	<u>0.9310</u>
<u>ETEX-1</u>	<u>Group 1 (real observations)</u>	<u>Before filtering</u>	<u>10.9936</u>	<u>0.3414</u>	<u>0.1000</u>	<u>0.2167</u>
		<u>After filtering</u>	<u>6.6769</u>	<u>0.5145</u>	<u>0.2500</u>	<u>0.3667</u>
	<u>Group 2 (real observations)</u>	<u>Before filtering</u>	<u>5.8705</u>	<u>-0.2824</u>	<u>0.0667</u>	<u>0.1167</u>
		<u>After filtering</u>	<u>4.9799</u>	<u>-0.2695</u>	<u>0.1167</u>	<u>0.2500</u>

3.2 Optimization of XGBoost model

3.2.1 Hyperparameters

Table S1 summarizes the optimal hyperparameters and corresponding GCs used for ~~source localization~~ source location estimation in this study; Tables S2–S5 includes all the optimal hyperparameters used in the 50 runs of the SCK-CEN ⁴¹Ar and ETEX-1 experiments. The optimal GCs of the SCK-CEN ⁴¹Ar experiment are smaller than those of the ETEX-1 experiment, indicating better fitting performance. This is because the sparse observations of the ETEX-1 experiment (Fig. S3) are more sensitive to the added Gaussian noise (see Sect. 2.5.2). ~~The optimal GC on Oct. 3 is smaller than that on Oct. 4, indicating better fitting performance. This difference is possibly the result of the larger training dataset for Oct. 3.~~

3.2.2 Feature selection

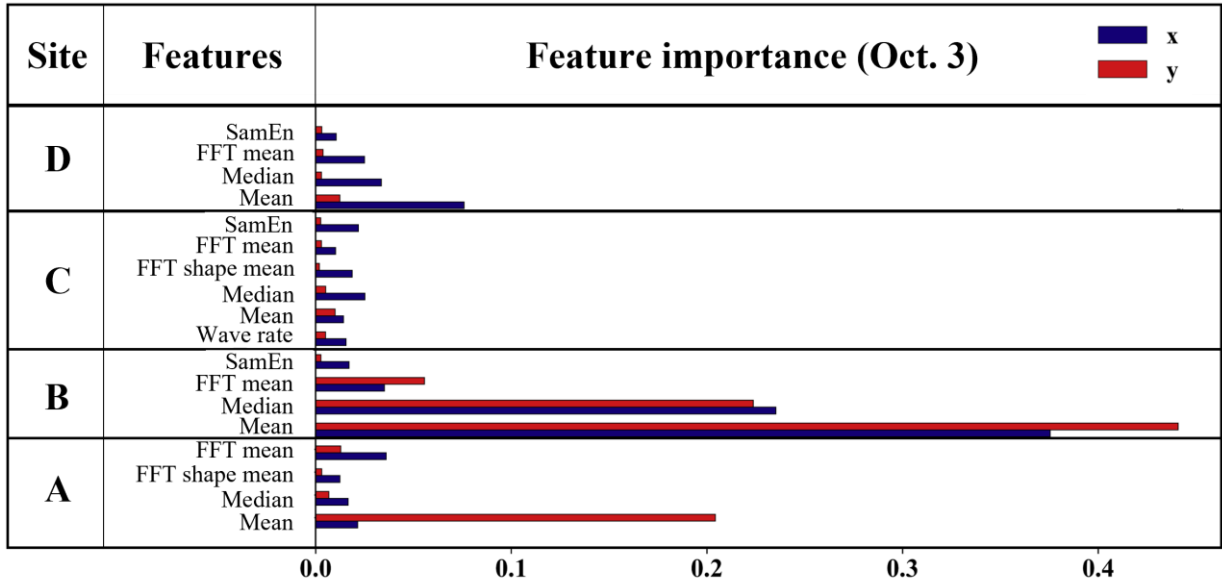
Figure 4 compares the importance of the selected features at each site for the two experiments. The time-domain features are dominant for both days in the SCK-CEN ⁴¹Ar experiment (Fig. 4a and 4b). For Oct. 3, Site B is the most important, possibly because it is farthest away in the crosswind direction. For Oct. 4, the four sites provide redundant feature information, and many features are removed. This is because the distribution of observation sites is almost parallel to the wind direction on this day. According to Fig. S3(b), the measurements from Sites A and B have a high correlation, thus leading to the removal of features from Site A on Oct. 4. In summary, the feature selection process adapts XGBoost to different application scenarios. Figure S4(a) and S4(b) shows the variations in MCV with the number of features for the x and y coordinates. The MCV first increases with the number of features, and then decreases slightly after reaching the maximum. The optimal number of features for Oct. 4 is noticeably smaller than for Oct. 3. In addition, the selected features for Oct. 3 involve all four sites, whereas those for Oct. 4 involve three sites. The reduced features and site numbers indicate a high level of redundancy in the observations acquired on Oct. 4. This is because the observation sites are parallel to the downwind direction and provide similar location information in the crosswind direction.

For the ETEX-1 experiment, Fig. 4c and d shows that the features of Group1 and Group2 are largely preserved after the feature selection process (only one feature is removed for each case), indicating less redundancy than that in the SCK-CEN ⁴¹Ar experiment. The time-domain features are dominant, but the frequency-domain features at some sites (e.g. D16 and S09) also play important roles. The MCVs of the ETEX-1 experiment have similar variation trends as those for the SCK-CEN ⁴¹Ar experiment (Fig. S4c and S4d). Figure S4 shows the variation of MCV with the number of features for the x and y coordinates. The MCV first increases with the number of features, and then decreases slightly after reaching the maximum for both days. The optimal number of features for Oct. 4 is noticeably smaller than for Oct. 3. In addition, the selected features for Oct. 3 involve all four sites, whereas those for Oct. 4 involve three sites for x and two sites for y. The reduced feature and site numbers indicate a high level of redundancy in the observations acquired on Oct. 4. This is because the observation sites are parallel to the downwind direction and provide similar location information in the crosswind direction.

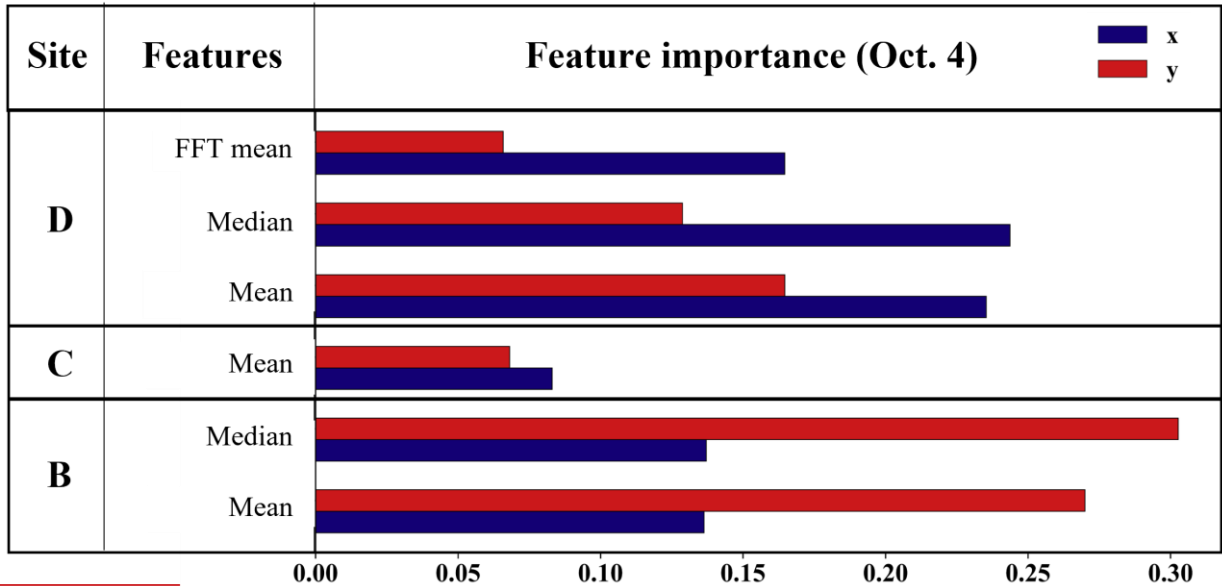
Figure 4 compares the importance of the selected features at each site. For both days, the temporal features are dominant.

454 For Oct. 3, Site B is the most important, possibly because it is farthest away in the crosswind direction. For Oct. 4, the four
 455 sites provide redundant feature information, and many features are removed. This is because the distribution of observation
 456 sites is almost parallel to the wind direction on this day. According to Fig. S3, the measurements from Site A and B have a high
 457 correlation, thus leading to the removal of features from Site A on Oct. 4. In summary, the feature selection process adapts
 458 XGBoost to different application scenarios.

(a)

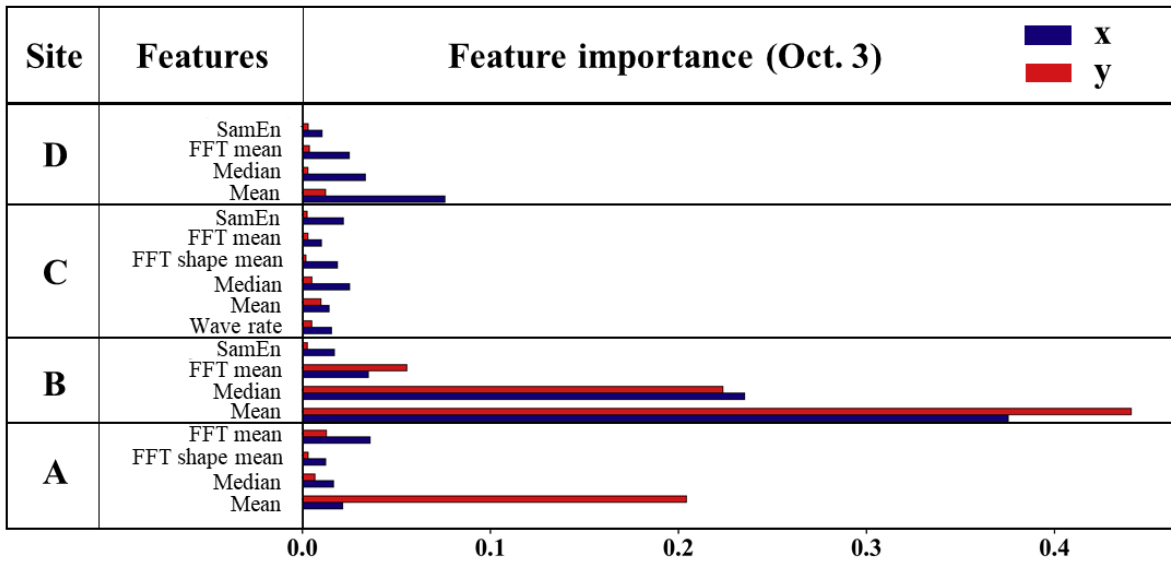


(b)

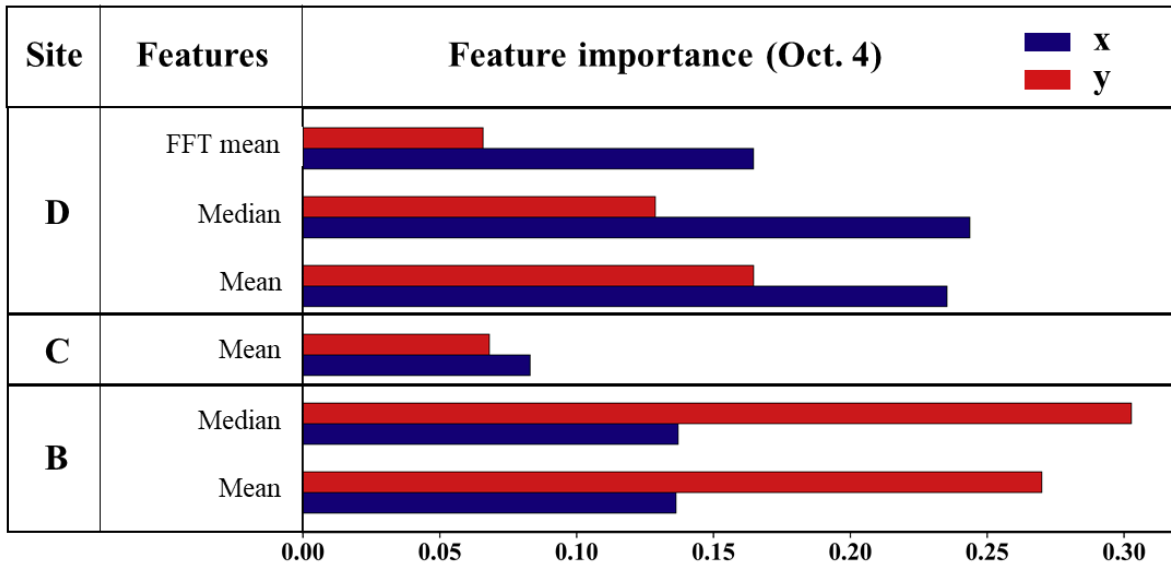


459

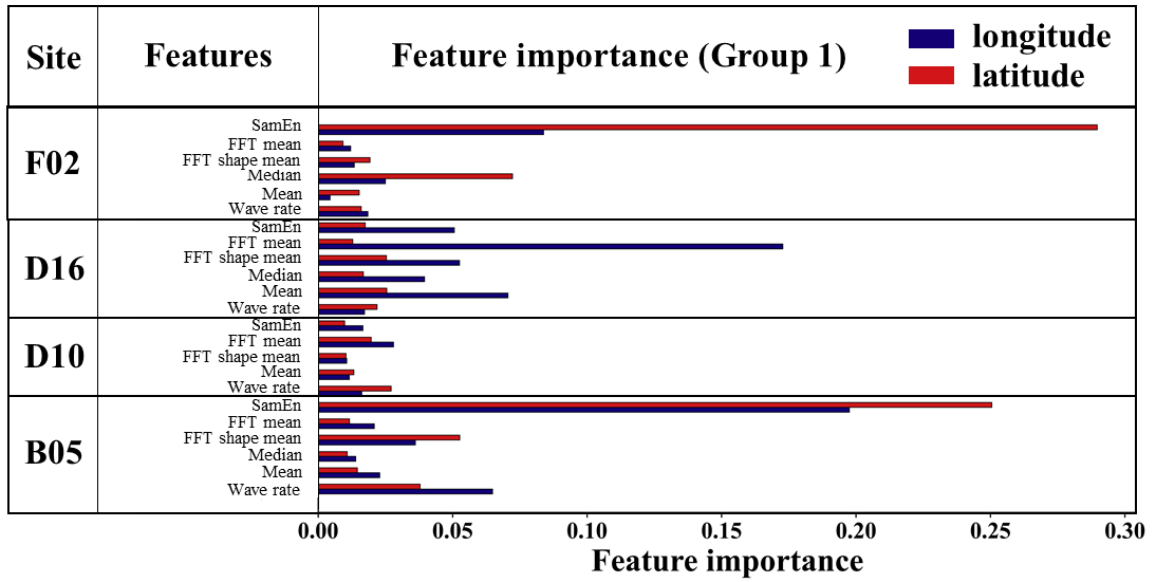
(a)



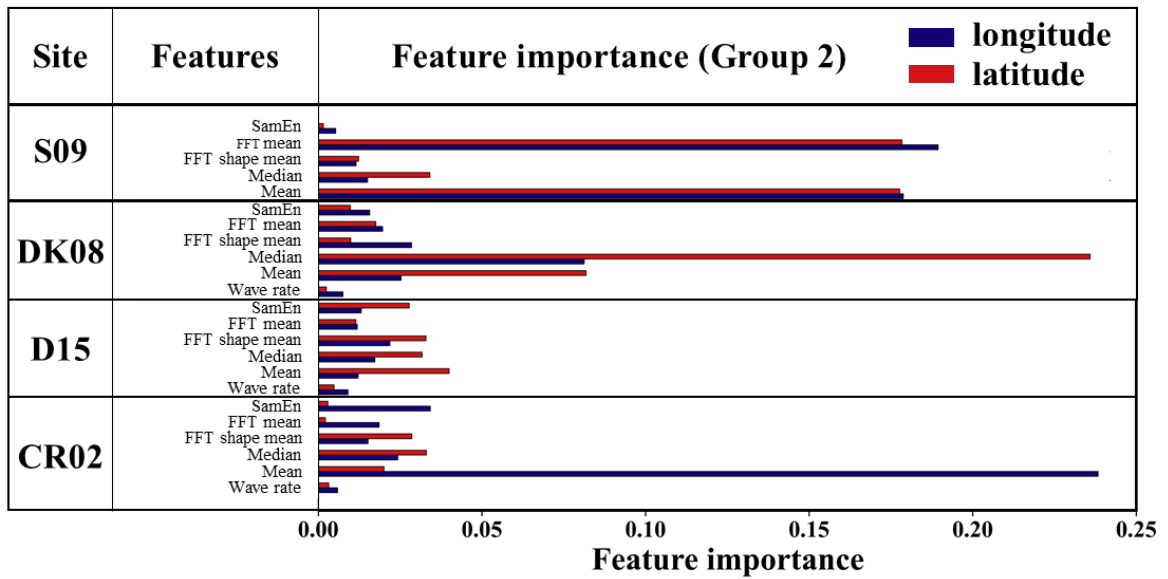
(b)



(c)



(d)



461

462

Figure 4. Feature importance of SCK-CEN ⁴¹Ar experiment: (a) Oct. 3; (b) Oct. 4; and ETEX-1 experiment: (c) Group 1; (d) Group 2.

463

3.3 Source reconstruction

464

3.3.1 Localization Source locations

465

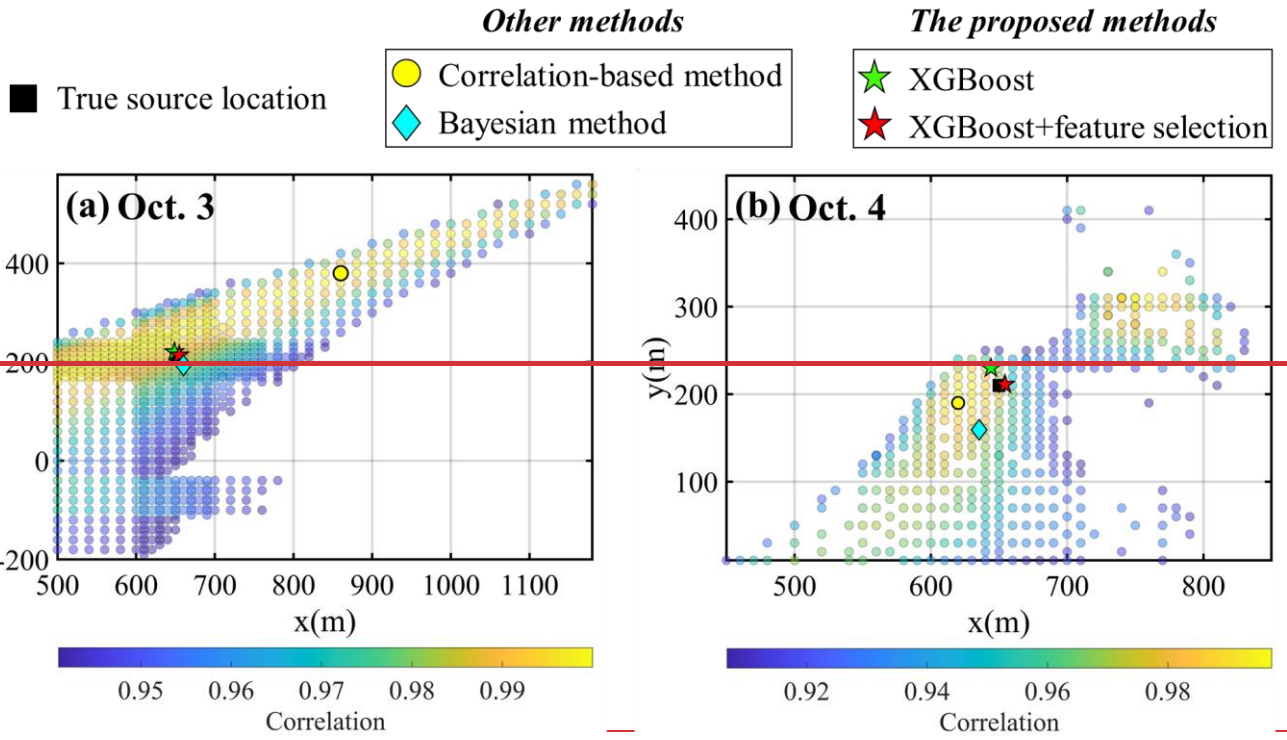
Figure 5 compares the best-estimated source locations of the correlation-based method, the Bayesian method, and the proposed

466

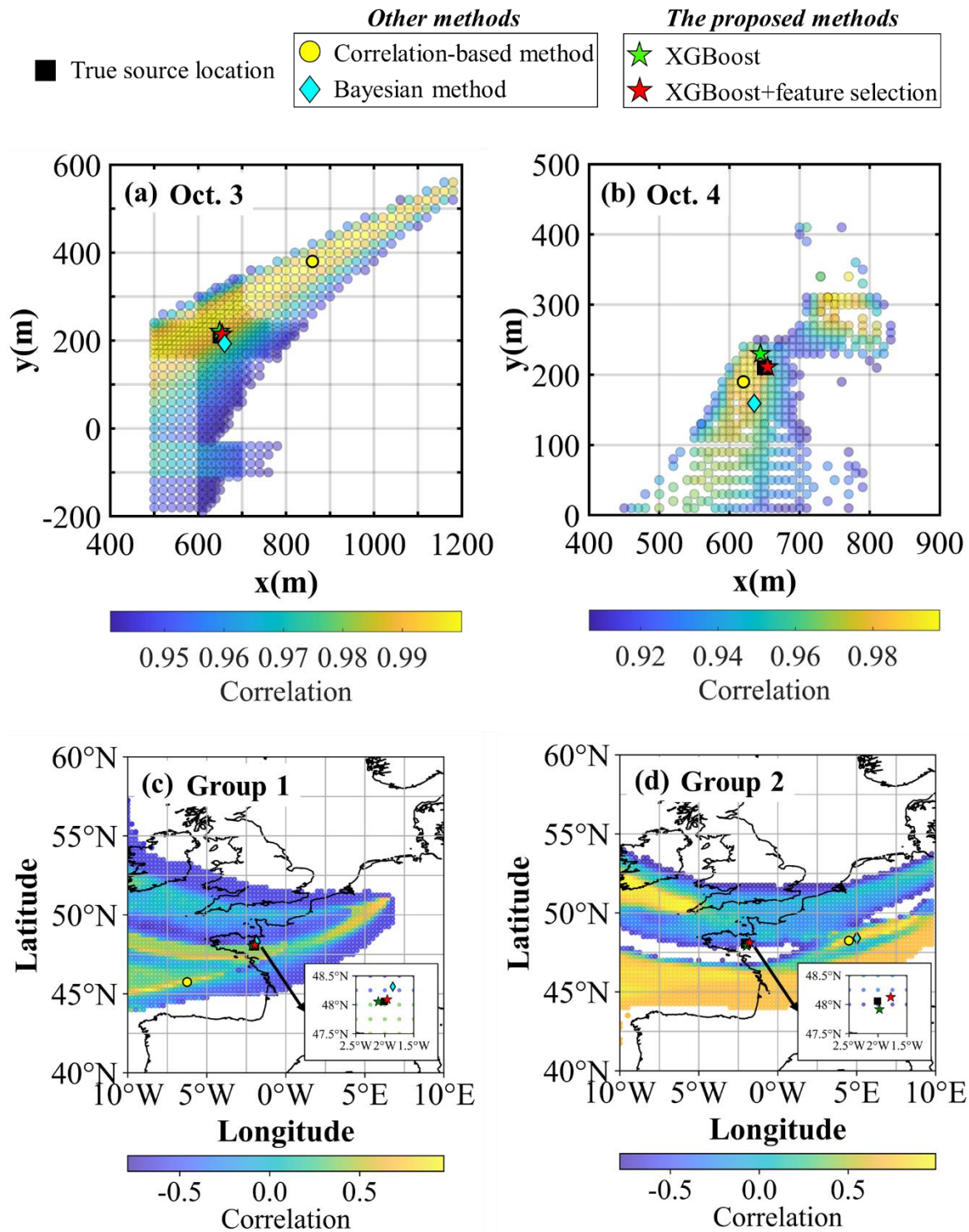
method with the ground truth. The pre-screening zone covers the true source location for both days, but the areas with the

467 highest correlation coefficients are still too large for the point source to be accurately located. The locations with the maximum
468 correlation exhibit errors of 270.19 m and 36.06 m for Oct. 3 and Oct. 4, respectively, indicating that the correlation-based
469 method may produce biased results in the case of non-constant releases. The Bayesian method estimates the location with
470 errors of 19.62 m and 52.81 m for Oct. 3 and Oct. 4, respectively. In comparison, the proposed method achieves the best
471 performance ~~among all the methods~~. The estimates without feature selection are only 10.65 m (Oct. 3) and 20.62 m (Oct. 4)
472 away from the true locations. Feature selection further reduces these errors to 6.19 m (Oct. 3, a relative error of 0.60%) and
473 4.52 m (Oct. 4, a relative error of 0.80%), which are below the grid size (10 m \times 10 m) of the ATDM-atmospheric dispersion
474 simulation. The ability to estimate the source location with accuracy surpassing the grid size can be attributed to the strong
475 fitting capability of the optimized XGBoost model (Chen and Guestrin, 2016; Grinsztajn et al., 2022). However, this capability,
476 although inherent, is not present across all optimized XGBoost models, as external factors such as observation noises and
477 meteorological data inaccuracies can also impact the accuracy of source location estimation.

478 For the ETEX-1 experiment, the pre-screening zone also covers the true source location for Group 1 and Group 2. The
479 source locations estimated by the correlation-based method are 411.85 km and 486.41 km away from the ground truth for
480 Group 1 and Group 2, respectively. The location error of the Bayesian method estimates is only 30.50 km for Group 1, but
481 increases to 520.77 km for Group 2, indicating the sensitivity of this method to the observations. In contrast, the proposed
482 method achieves much lower source location errors of 5.19 km for Group 1 (a relative error of 0.20%) and 17.65 km for Group
483 2 (a relative error of 0.70%). Group 1 exhibits a lower source location error than Group 2, because the observation sites of
484 Group 1 are closer to the sampled source locations than those of Group 2 and better characterize the plume. Feature selection
485 did not remove many features (Fig. 4c and 4d), so the estimated source locations with and without feature selection basically
486 overlap for both groups. The proposed method gives a relative error of less than 0.9% for both days, whereas the Bayesian
487 method produces a relative error of above 11% and that of the correlation based method can be as high as 26%. The best
488 estimates for Oct. 3 are more accurate than those for Oct. 4, possibly because of the better layout of observation sites (Fig. 2)
489 and the better decoupling results (Fig. 3).



490



491

492

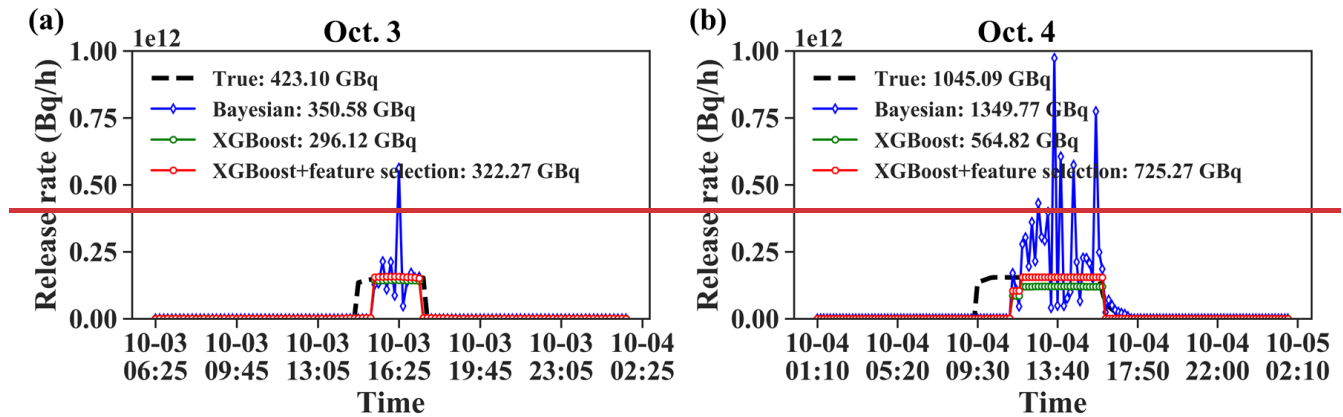
Figure 5. Source localization results of SCK-CEN ⁴¹Ar experiment: (a) Oct. 3; (b) Oct. 4; and ETEX-1 experiment:

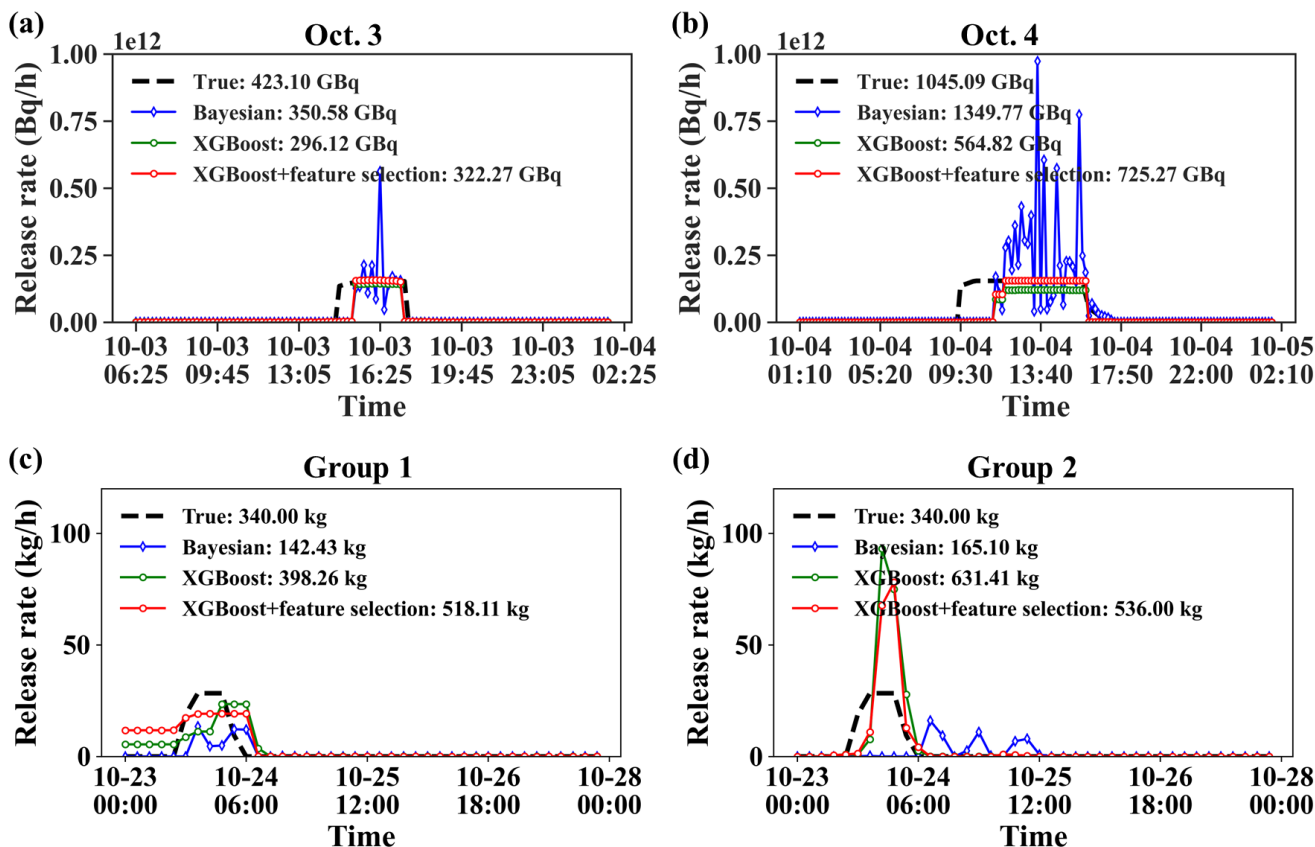
(c) Group 1; (d) Group 2. A detailed enlargement of the region around (2.5°W, 47.5°N) to (1.5°W, 48.5°N) is shown in the bottom right corner in (c) and (d) to highlight the source location estimation results of the proposed method. The yellow dots denote the maximum correlation points, which are the localization results of the correlation-based method. The green and red stars represent the localization results based on XGBoost before and after feature selection, respectively. The cyan diamonds represent the localization results based on the Bayesian method. (a) Oct. 3; (b) Oct. 4.

3.3.2 Release rates

Figure 6 displays the release rates estimated by the Bayesian and PAMILT methods based on the source localization source location estimates results in Fig. 5. For the SCK-CEN ^{41}Ar experiment (Fig. 6a and 6b), the release rates provided by the Bayesian method present several sharp peaks, corresponding to overestimates of up to 269.03% (Oct. 3) and 532.35% (Oct. 4). Furthermore, the Bayesian estimates exhibit unrealistic oscillations in the stable release phase. In contrast, the PAMILT method successfully retrieves the peak releases without oscillations for both days. Both the Bayesian and PAMILT estimates give delayed release start times, but accurately estimate the end times, especially for Oct. 3. The PAMILT estimate underestimates the total release by 30.01% and 45.95% for Oct. 3 and Oct. 4, respectively; these values are reduced to about 23.83% and 30.60%, respectively, after feature selection. The Bayesian method gives better total releases because of the overestimated peaks.

For the ETEX-1 experiment (Fig. 6c and 6d), the Bayesian estimates exhibit notable fluctuations, leading to underestimations of 58.11% for Group1 and 51.44% for Group 2. Furthermore, the temporal profile of the Bayesian estimates for Group 2 falls completely outside the true release window. In contrast, most releases using the PAMILT estimates are within the true release time window, especially for Group 2, despite the overestimations reaching 52.38% for Group 1 and 57.65% for Group 2, after the feature selection process. Compared with the SCK-CEN ^{41}Ar experiment, the increased deviation in the ETEX-1 experiment is caused by the sparsity of observations at the four sites (Fig. S3).



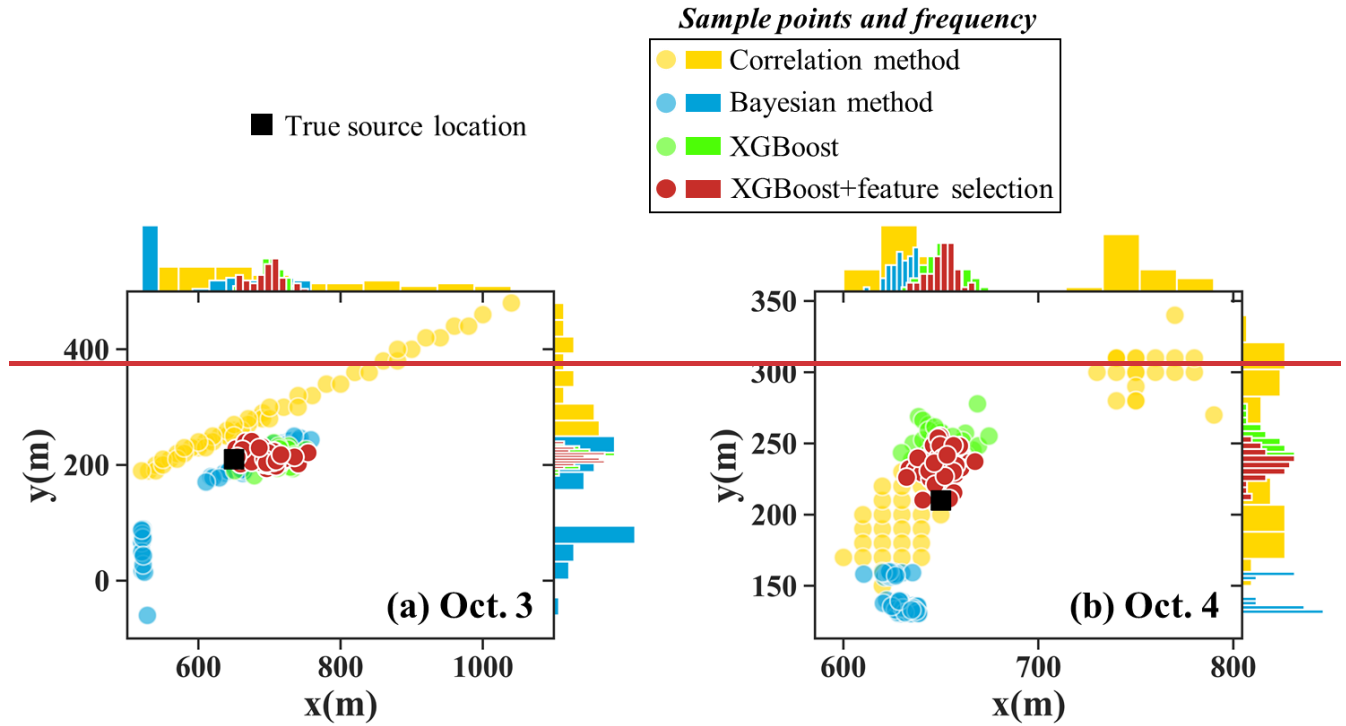


515
 516 **Figure 6.** Release rate estimation results with different location estimates of SCK-CEN ^{41}Ar experiment: (a) Oct. 3; (b) Oct. 4; and ETEX-
 517 1 experiment: (c) Group 1; (d) Group 2. The release rates labelled XGBoost or XGBoost+feature selection are estimated using the PAMILT
 518 method. The rectangles inside each figure present the location estimates used in the release rate estimations. The green and red stars denote
 519 the source locations estimated by XGBoost without and with feature selection, respectively.

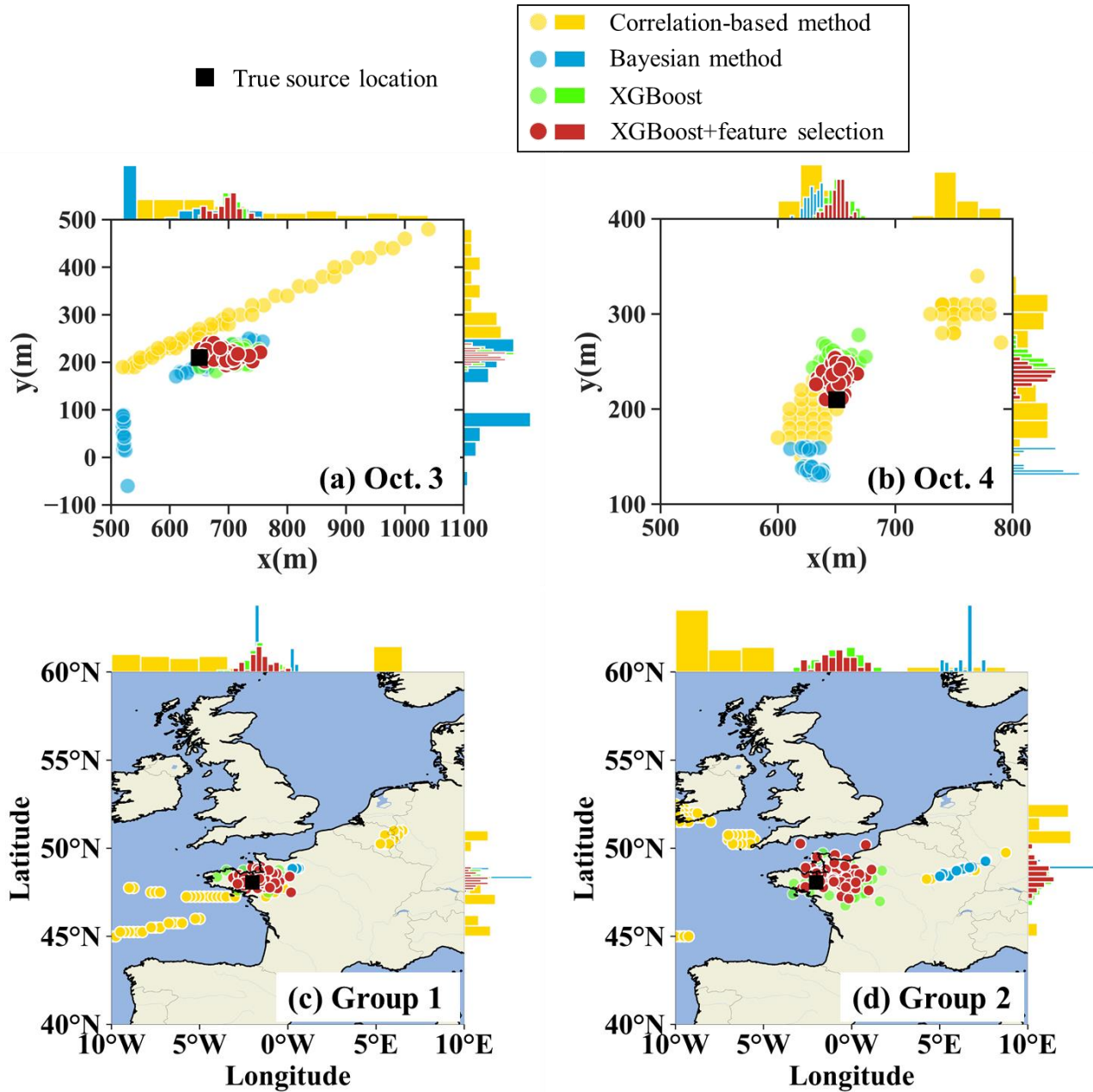
520 3.3.3 Uncertainty range

521 Figure 7 compares the spatial distribution of 50 estimates produced by the different source localization methods. For the SCK-
 522 CEN ^{41}Ar experiment, the estimates of the correlation-based method are highly spread-dispersed for both days, leading to
 523 a highly-very uniform distribution of the x coordinate for Oct. 3 and two separate distributions of both the coordinates for Oct.
 524 4. The Bayesian method produces a multimodal distribution for both days, in which the estimates are more concentrated than
 525 those of the correlation-based method. The corresponding full posteriori distributions in Fig. S5(a) and S5(b) better reveal the
 526 multimodal feature of the Bayesian method, with several peaks of similar probabilities in the estimates of both coordinates on
 527 Oct. 3 and the y coordinate on Oct. 4. The multimodal feature indicates the difficulty of constraining the solution in
 528 simultaneous spatiotemporal reconstruction, as reported in a previous study (Meutter and Hoffman, 2020). In comparison, the
 529 proposed method provides the most concentrated source location estimates. The feature selection moves the centre of the
 530 distribution closer to the true location and narrows the distribution of the estimates, especially for Oct. 4.

531 For the ETEX-1 experiment, the estimates of the correlation-based method are quite dispersed, whereas those of the
532 Bayesian method are more concentrated. The Bayesian estimates are close to the truth for Group 1, but deviate noticeably for
533 Group 2. This phenomenon indicates that the Bayesian method is sensitive to the observations, especially when the
534 observations are sparse. Figure S5(c) and S5(d) reveals that the Bayesian-estimated posterior distribution is multimodal for
535 both ETEX-1 groups; this can be avoided by using additional observations (Fig. S5e). In contrast, the proposed method
536 provides estimates that are concentrated around the truth for both Group 1 and Group 2, indicating its efficiency in the case of
537 sparse observations. Due to the shorter distance between observation sites and the sampled source locations, the uncertainty
538 range of source location for Group 1 is narrower than that for Group 2.



Estimates and frequency distribution



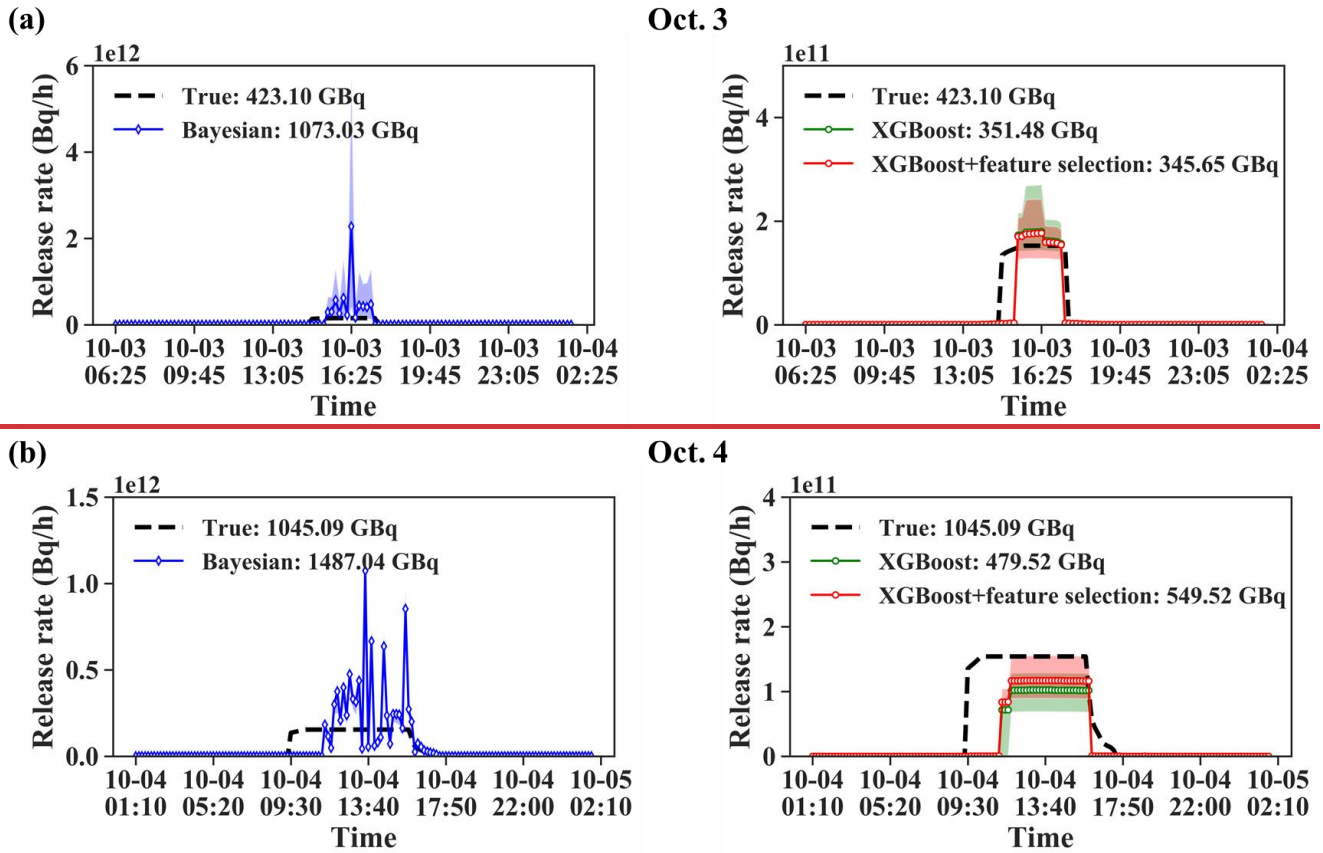
540

541 **Figure 7.** Spatial distribution of 50 source location estimates of SCK-CEN ^{41}Ar experiment: (a) Oct. 3; (b) Oct. 4; and ETEX-1 experiment:
 542 (c) Group 1; (d) Group 2. Each circle denotes an individual estimate as detailed in Sect. 2.8.5, with colour variations indicating the respective
 543 method employed. Histograms along the axes represent the frequency distribution of the estimates along the respective axis. Distribution of
 544 source localization results over 50 calculations. (a) Oct. 3; (b) Oct. 4.

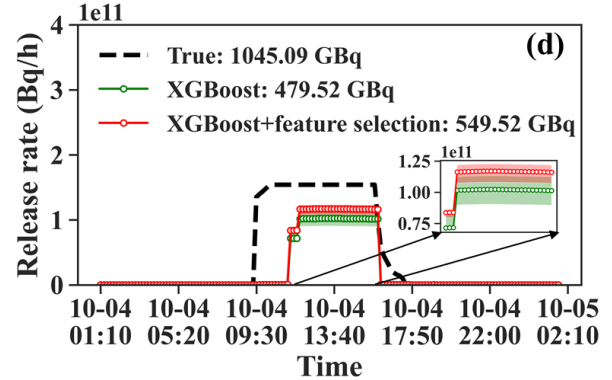
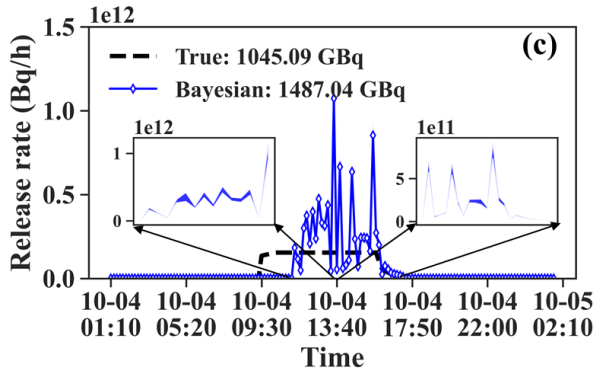
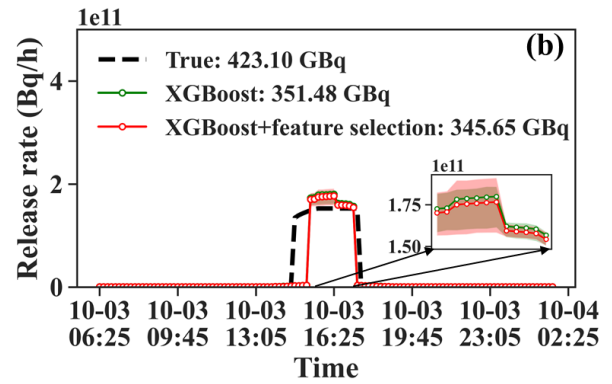
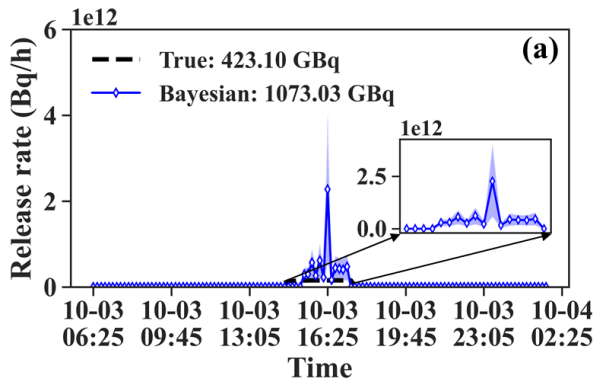
545

Figure 8 compares the uncertainty range and the mean total release of the release rate estimations for the SCK-CEN ^{41}Ar

546 experiment. For Oct. 3, the Bayesian estimates significantly overestimate the mean values and have a large uncertainty range,
 547 whereas the mean PAMILT estimate is very close to the true release and the uncertainty range is smaller than that of the
 548 Bayesian method. For Oct. 4, the mean Bayesian estimate exhibits more-greater deviations than the mean PAMILT estimate.
 549 Feature selection improves the mean estimate and reduces the uncertainty range of PAMILT because it improves the source
 550 localizationsource location estimation, thus reducing the deviation in the inverse model of the release rate. On Oct. 3 and Oct.
 551 4, the PAMILT method underestimates the total release by 18.30% and 47.42%, respectively, whereas the Bayesian method
 552 gives overestimations of 153.61% and 42.29%, respectively. ~~These results demonstrate that the PAMILT method is robust to~~
 553 ~~localization deviations and can reconstruct the timing, peaks, and total release with relatively high accuracy. This robustness~~
 554 ~~reduces the propagation of localization errors to the release rate estimation, and improves the accuracy of spatiotemporally~~
 555 ~~decoupled source reconstruction.~~



556



557
558 **Figure 8.** Release rate estimates over 50 calculations of SCK-CEN ^{41}Ar experiment. (a) Oct. 3-Bayesian method; (b) Oct. 3-PAMILT method;
559 (c) Oct. 4-Bayesian method; (d) Oct. 4-PAMILT method. The shadow represents the uncertainty range between the lower quartile and the
560 upper quartile. The shadow of each figure is amplified by an enlarged subgraph. The legends in each figure provide the mean estimates for
561 the total release. (a) Oct. 3; (b) Oct. 4. The shadow represents the release rate range between the minimum and the maximum.

562 Figure 9 compares the uncertainty ranges of the release rate estimates for the two ETEX-1 groups. For both groups, the
563 Bayesian estimates exhibit noticeable underestimations (including the mean estimate) and small uncertainty ranges (Fig. 9a
564 and 9c). The Bayesian estimates fall completely outside the true release window for Group 2 (Fig. 9c). The mean PAMILT
565 estimates are more accurate than the mean Bayesian estimates, with most releases within the true release window (Fig. 9b and
566 9d). However, the PAMILT estimates have a large uncertainty range for the ETEX-I experiment than for the SCK-CEN ^{41}Ar
567 experiment, implying that the source-receptor matrices of the ETEX-1 experiment are more sensitive to errors in source
568 location than those of the SCK-CEN ^{41}Ar experiment. This greater sensitivity originates from the complex meteorology in the
569 ETEX-1 experiment. As for the mean total releases, the Bayesian method produces underestimations of 70.93% for Group 1
570 and 74.15% for Group 2. In comparison, the proposed method gives deviations of only 0.71% for Group 1 and 0.09% for Group
571 2, after feature selection.

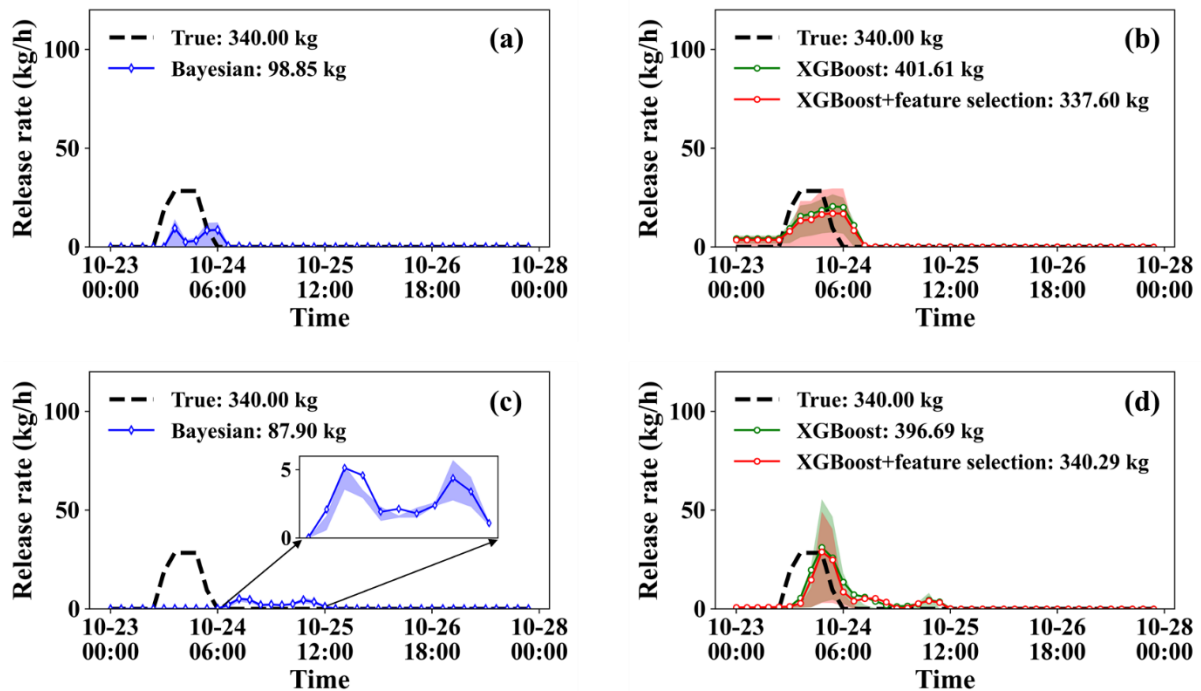


Figure 9. Release rate estimates over 50 calculations of ETEX-1 experiment. (a) Group 1-Bayesian method; (b) Group 1-PAMILT method; (c) Group 2-Bayesian method; (d) Group 2-PAMILT method.

Table 3 Table 4 lists the mean and standard deviation of the relative errors for the 50 estimates given by the various different methods. The correlation-based method produces the largest mean relative error and standard deviation for source location estimation, except for Group 2 of ETEX-I. For the SCK-CEN ^{41}Ar experiment, the In terms of source localization, the correlation-based method produces the largest mean relative error and standard deviation. The proposed method gives the smallest mean error, about half of that of the Bayesian method. Its standard deviation is three fold smaller than around one-quarter of that of the Bayesian method for Oct. 3, but is slightly larger for Oct. 4. For the total release, the PAMILT method gives a better standard deviation of the relative error for both days and a better mean relative error for Oct. 3, whereas the Bayesian method produces a better mean relative error for Oct. 4. Feature selection reduces the mean relative error, except for the total release for Oct. 3, and slightly increases the standard deviation of the source location and the total release results for Oct. 3. The mean relative error of the total release averaged on the two days is 65.09% lower than that of the Bayesian method.

For the ETEX-1 experiment, the Bayesian method exhibits case-sensitive performances with respect to the mean relative error of source location estimation, whereas the proposed method gives the most accurate source locations with small uncertainties for both groups. As for the total release, the proposed method gives smaller mean relative errors than the Bayesian methods, but the Bayesian method has a smaller standard deviation. Feature selection significantly reduces the mean relative error for the two groups. The mean relative error of the total release averaged over the two groups is 72.14% lower than that of the Bayesian method.

591
592

Table 4. Relative errors of source reconstruction. δ_r represents the relative error of source location, which is positive and δ_Q denotes the relative error of total release, where a positive value indicates overestimation and a negative value denotes underestimation.

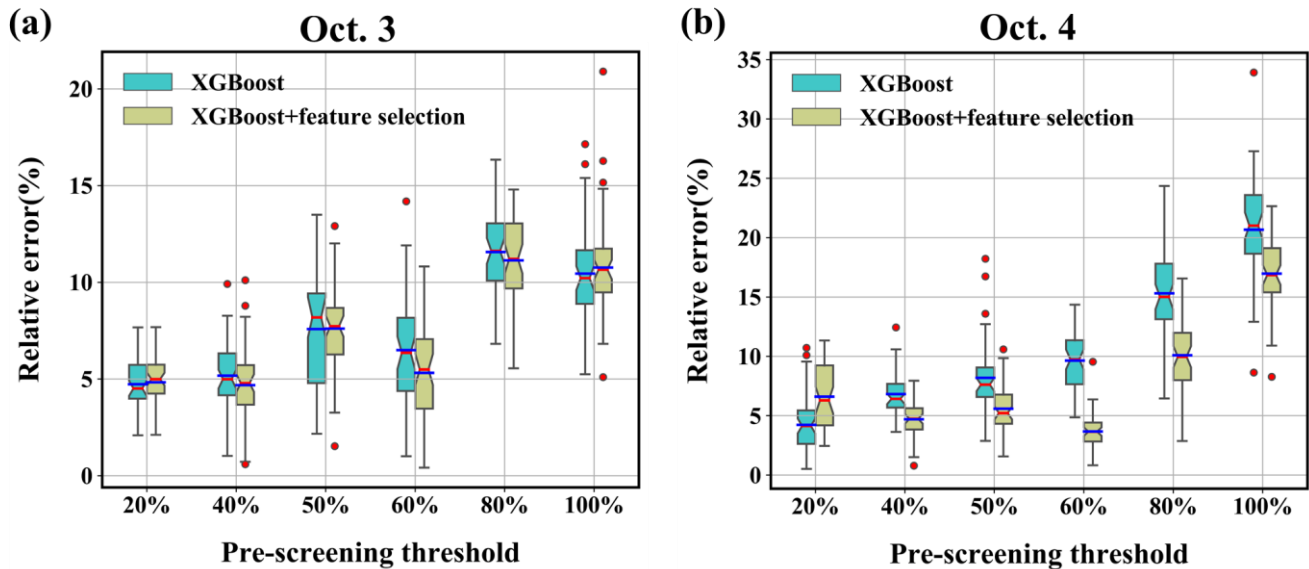
Experiment	Case	Statistical parameters (Relative error)	Correlation-based method	Bayesian method	The proposed method			
					XGBoost	XGBoost+ feature selection		
SCK-CEN ⁴¹ Ar	Oct. 3	δ_r	Mean	14.10%	11.88%	5.18%	4.68%	
			Std	11.37%	7.53%	1.79%	2.05%	
		δ_Q	Mean	-	153.61%	-16.93%	-18.30%	
			Std	-	189.76%	9.45%	8.01%	
	Oct. 4	δ_r	Mean	14.30%	12.83%	6.83%	4.71%	
			Std	9.60%	1.68%	1.76%	1.53%	
		δ_Q	Mean	-	42.29%	-54.12%	-47.42%	
			Std	-	15.05%	6.47%	5.85%	
	ETEX-I	Group 1	δ_r	Mean	16.95%	3.22%	2.32%	2.42%
				Std	7.46%	2.75%	1.43%	1.43%
δ_Q			Mean	-	-70.93%	18.12%	-0.71%	
			Std	-	17.87%	99.85%	102.01%	
Group 2		δ_r	Mean	21.9%	23.97%	5.21%	4.97%	
			Std	5.05%	1.97%	2.42%	2.35%	
		δ_Q	Mean	-	-74.15%	16.67%	0.09%	
			Std	-	11.68%	93.50%	109.56%	

3.4 Sensitivity analysis results

3.4.1 Sensitivity to the search range

Figure 9–Figure 10 displays the localization–source location errors obtained using different pre-screening thresholds to determine the search range. The error is smaller with a lower threshold, implying that a small pre-screening range search range helps reduce the mean and median errors. As the threshold increases, the mean and median errors, as well as the error range, show an overall tendency to increase, but not in a strictly monotonic way. The mean/median error is less than 12% for Oct. 3 and less than 22% for Oct. 4, indicating robust performance in these tests. Feature selection reduces the mean/median, range, and the lower bound of the errors in most tests, demonstrating its efficiency.

600

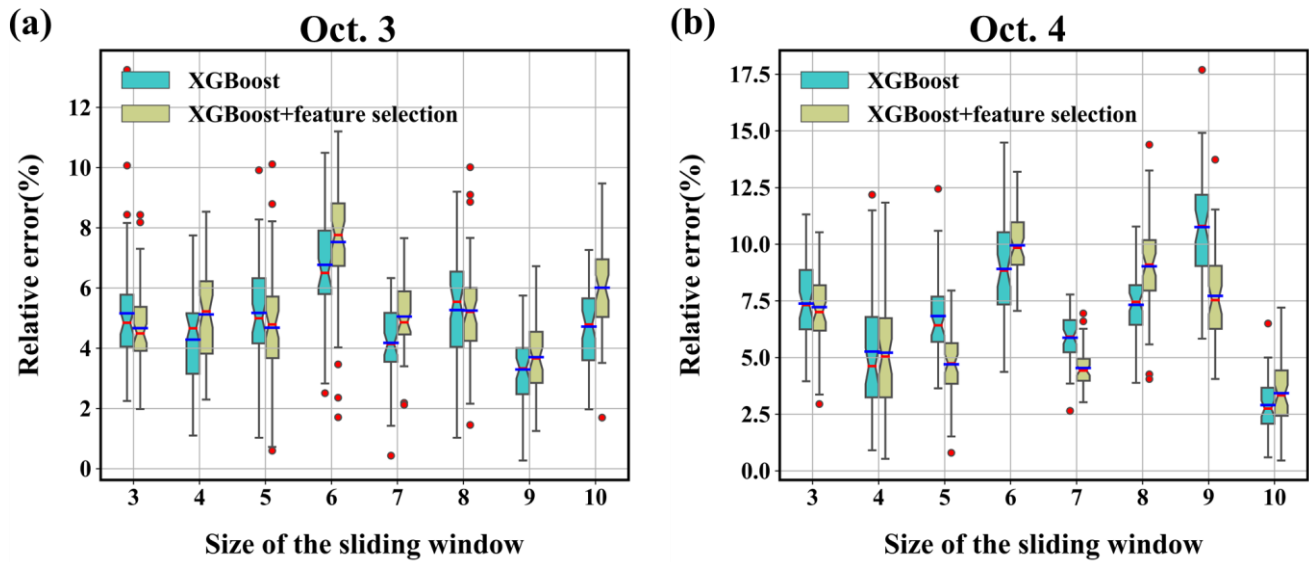


601

602 **Figure 9** **Figure 10.** Distribution of relative error (%) over 50 runs with different search ranges. The blue and red solid lines denote average
 603 relative error (%) and median relative error (%), respectively. The upper and lower boundaries represent the upper and lower quartiles of
 604 relative error (%), respectively. The fences are 1.5 times the inter-quartile ranges of the upper/lower quartiles. The red circles denote data
 605 that are not included between the fences. (a) Oct. 3; (b) Oct. 4.

606 3.4.2 Sensitivity to the size of the sliding window

607 **Figure 10** **Figure 11** shows the localization-source location errors obtained with different sliding-window sizes. The
 608 mean/median error is less than 8% for Oct. 3 and less than 11% for Oct. 4, both of which are smaller than for the various pre-
 609 screening ranges search ranges. This indicates that the proposed method is more robust to this parameter than to the pre-
 610 screening ranges search range. For both days, the lowest mean/median and error range occur with relatively large window sizes,
 611 i.e. window size of 9 for Oct. 3 and window size of 10 for Oct. 4. This is because a large window size increases the strength
 612 of the decoupling-filtering and removes the temporal variations of-in the release rates more completely. However, a large
 613 window size leads to increased computational cost. Because the errors vary in a limited range, a medium window size provides
 614 a better balance between accuracy and computational cost. Feature selection improves the results for medium and small
 615 window sizes, but may have less effect with large window sizes. This tendency implies that it is more appropriate to apply
 616 feature selection with medium window sizes than with large window sizes, as is done in this study.

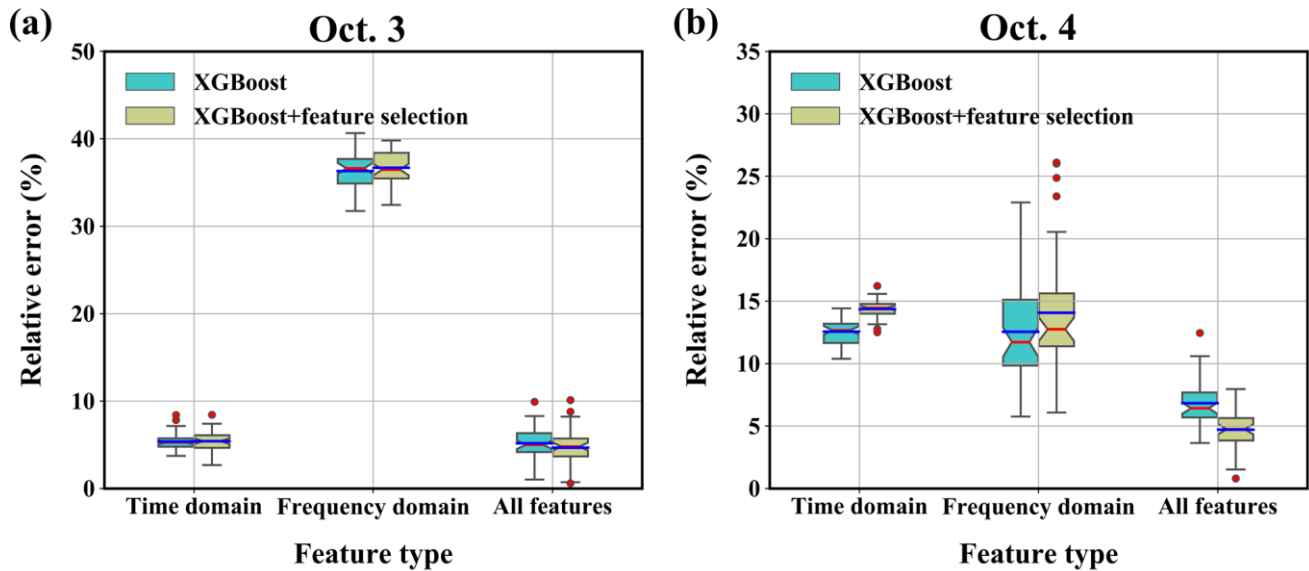


617

618 **Figure 10** **Figure 11**. Sensitivity to the size of the sliding window. (a) Oct. 3; (b) Oct. 4.

619 3.4.3 Sensitivity to the feature type

620 **Figure 11** **Figure 12** compares the results obtained with different feature types. For Oct. 3, the localization-source location errors
 621 are quite low when using only the time-domain features for the reconstruction; indeed, the errors are only slightly larger than
 622 when using all the features. In contrast, the results obtained using only the frequency-domain features exhibit noticeably-larger
 623 errors, indicating that the time-domain features make a greater contribution to the results for Oct. 3. For Oct. 4, the mean
 624 localization-source location errors are similar when using the features of either the time- or frequency-domain features, but
 625 the error range is higher when the frequency-domain features are used. In addition, the errors of both single-domain-feature
 626 results are higher than those of the all-feature results, indicating that both feature types should be considered included to ensure
 627 accurate and robust source localization source location estimation.

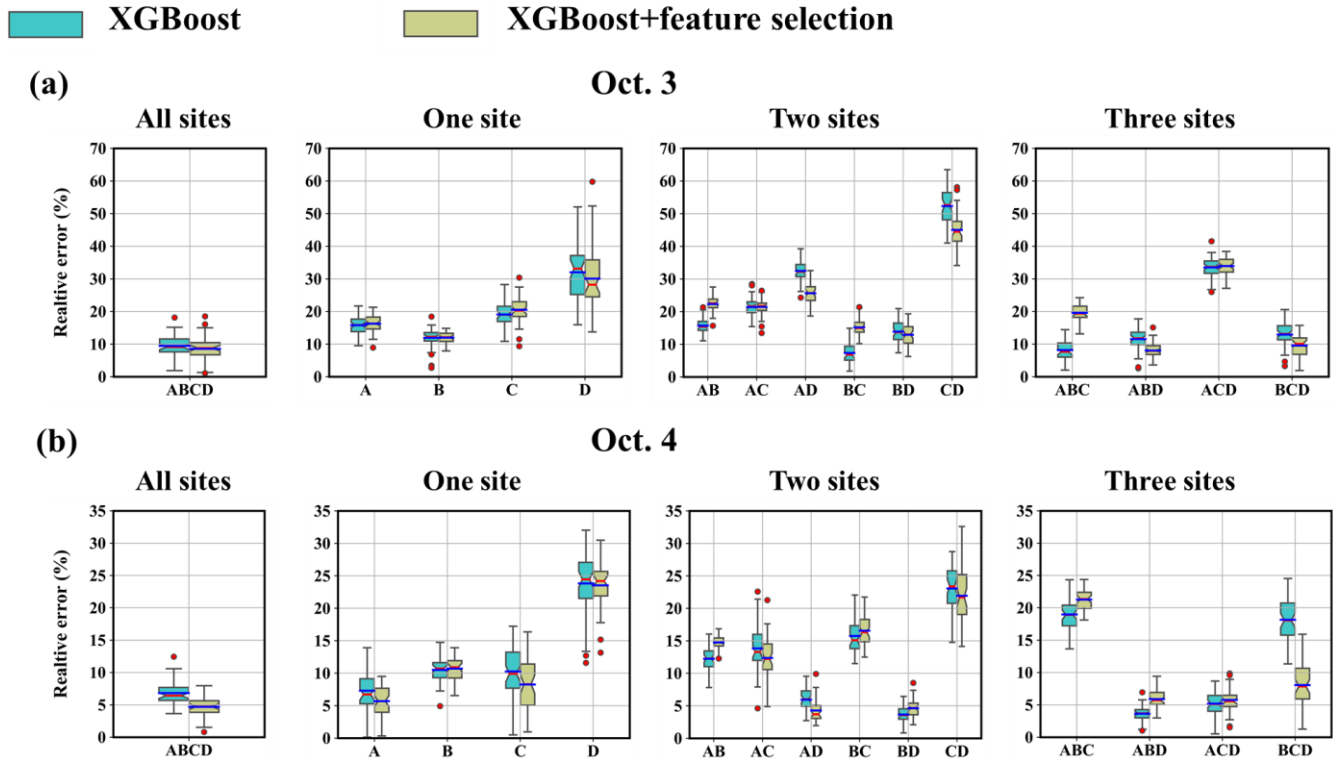


628 **Figure 12**. Sensitivity to the feature type. (a) Oct. 3; (b) Oct. 4.

630 3.4.4 Sensitivity to the number and combination of observation sites

631 **Figure 13** compares the results obtained with different numbers and combinations of observation sites. The results
 632 indicate that the localization-source location error may be more sensitive to the position of the observation site than to the
 633 number of sites included. The error level of all-site estimations is relatively low for both days, indicating that increasing the
 634 number of observation sites better constrains the solution and help improve the robustness of the model. However, the lowest
 635 error levels are achieved by a subset of sites, i.e. Site ABD on Oct. 3 and Site BD on Oct. 4. This is possibly because including
 636 all observation sites may cause overfitting and reduce the prediction accuracy. This overfitting can be alleviated by using only
 637 representative sites at appropriate position, which capture the environmental variability and provide clear information for
 638 locating the source. For Oct.3, multi-site estimations with Site B always produce low error levels, and single-site estimation
 639 using Site B also achieves high accuracy. For Oct.4, multi-site estimations with Site BD always achieve relatively low error
 640 levels. These results demonstrate the importance of using representative sites for source location estimation. The representative
 641 sites (Site B for Oct. 3 and Site BD for Oct. 4) are consistent with the importance calculated in the feature selection step (Fig.
 642 4), preliminarily indicating the potential for feature selection to identify representative sites. In addition, feature selection
 643 reduces the mean error level in most cases. For both days, the results obtained using a subset of sites produce the lowest error
 644 level, i.e. Site ABD on Oct. 3 and Site BD on Oct. 4. These results are completely consistent with the feature importance results
 645 in Fig. 4. The implication is that sampling a plume at multiple locations with correspondingly different activity concentrations
 646 is more likely to result in a better reconstruction because the environmental variability is more fully captured through direct
 647 observations. For Oct. 3, source localization with Site B always produces lower error levels, though Site B is farthest away in
 648 the crosswind direction. However, the results on Oct. 4 do not exhibit the same phenomenon, mainly because almost all

649 observation sites are parallel to the downwind direction. In addition, the single-site results can also achieve low error levels,
 650 such as Site B on Oct. 3 and Site A on Oct. 4. Feature selection reduces the mean error level in most test cases. These results
 651 indicate that the proposed method may achieve satisfactory results with different numbers and combinations of observation
 652 sites. It also remains effective with very few observation sites, on the condition that the observations sufficiently capture the
 653 plume.

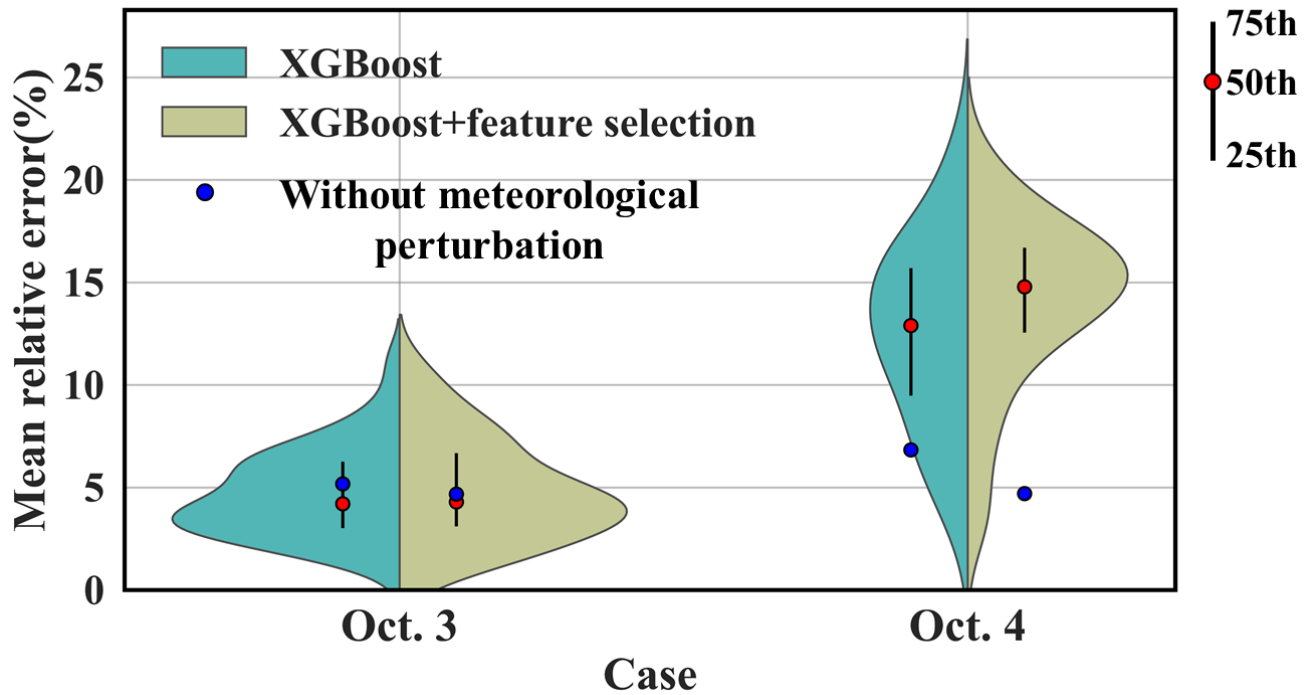


654 **Figure 12** **Figure 13.** Sensitivity to the number and combination of observation sites. (a) Oct. 3; (b) Oct. 4.

656 3.4.5 Sensitivity to the meteorological errors

657 Figure 14 illustrates the distribution of mean relative source location errors (averaged across 50 groups of hyperparameters)
 658 retrieved with 50 perturbed meteorological inputs. For Oct. 3, the estimates generally present a low error level (generally below
 659 10%), and the 50th error level is lower than the error of the unperturbed results (4.68%). In comparison, for Oct. 4, most
 660 perturbed results exhibit larger errors (primarily 10%–20%) than the unperturbed result (4.71%), indicating that models for
 661 Oct. 4 are more sensitive to the meteorological errors. This sensitivity difference results from the layout of the observation
 662 sites (Fig. 2a). The sites on Oct. 3 were almost perpendicular to the prevailing wind direction, capturing the plume under a
 663 large range of wind directions. In contrast, the sites on Oct. 4 were basically parallel to the wind direction, capturing the plume
 664 only for a very limited range of wind directions. This result indicates the importance of site layout for robust reconstruction in
 665 the presence of meteorological errors. Feature selection slightly changes the mean relative error distribution and its percentiles

666 for both days, indicating that meteorological errors may alter the importance of each feature and reduce the effectiveness of
667 feature selection. In addition to meteorological errors, dispersion errors such as wet deposition parameterization (Zhuang et
668 al., 2023) may influence the result, but these errors are not dominant in the two field experiments. The handling of such
669 dispersion errors will be investigated in future work.



670
671 **Figure 14.** Sensitivity to the meteorological errors. The violin plots illustrate the kernel density estimation of errors under different
672 meteorological groups for XGBoost models before and after feature selection. The vertical black lines inside the violins depict the
673 interquartile range, capturing the 25th, 50th (red dots), and 75th percentiles of mean relative errors. The blue dots denote the mean relative
674 source location errors for models without meteorological perturbation, as listed in Table 4.

675 4. Conclusions

676 In this study, we relaxed the unrealistic constant-release assumption of source reconstruction. Instead, we took advantage of
677 the fact that most atmospheric radionuclide releases have a spatially fixed source, and thus the release rate mainly influences
678 the peak values in the temporal observations. Based on this, a more general spatiotemporally ~~decoupled-separated~~ source
679 reconstruction method was developed to estimate non-constant releases. ~~Decoupling-The separation process~~ was achieved by
680 applying a temporal sliding-window average filter to the observations. This filter reduces the influence of temporal variations
681 in the release rates on the observations, so that the relative spatiotemporal distribution of the filtered observations is dominated
682 by the source location and known meteorology. A response feature vector was extracted to quantify the long-term temporal
683 response trends at each observation site, involving tailored indicators of both the time and frequency domains. The XGBoost

684 algorithm was used to train a machine learning model that links the source location to the feature vector, enabling independent
685 ~~source localization~~source location estimation without knowing the release rates. With the retrieved source location, the detailed
686 temporal variations of the release rate were determined using the PAMILT algorithm. Validation was performed against the
687 two-day SCK-CEN ^{41}Ar field experimental data and two groups of ETEX-1 data; ~~The~~and the results demonstrate that the
688 proposed method successfully removes the influence of temporal variations in release rates across observations and accurately
689 ~~localizes the source~~reconstructs both the spatial location and temporal variations of the source.

690 For the local-scale SCK-CEN ^{41}Ar experiment, source location was reconstructed with lowest errors of only 0.60% (Oct. 3)
691 and 0.80% (Oct. 4), significantly lower than for the correlation-based method and Bayesian method. Source localization was
692 achieved with deviations of only 4.68% and 4.71% on Oct. 3 and Oct. 4, respectively, representing reductions of 9.42% and
693 9.59%, respectively, compared with the results from a recent correlation-based method and 7.20% and 8.12%, respectively,
694 compared with the results from the Bayesian method. In terms of the release rate, the PAMILT method reconstructed the
695 temporal variations, peak, and total release with high accuracy, thus avoiding the unrealistic oscillations given by the Bayesian
696 estimate. The proposed method ~~also exhibited~~produced smaller uncertainty ranges ~~in terms of the source location and total~~
697 ~~release~~ than the Bayesian method, and avoided the multimodal distribution of the Bayesian method. The feature selection
698 process removed the redundant features and reduced the reconstruction errors. For the continental-scale ETEX-1 experiment,
699 the lowest relative source location errors were 0.20% and 0.70% for Group 1 and Group 2, respectively, which were again
700 lower than for the correlation-based and Bayesian methods. The proposed method provides highly accurate mean estimates of
701 the release rate for both groups, although with a large uncertainty range.

702 Sensitivity analyses on the SCK-CEN ^{41}Ar experiment revealed that the proposed method exhibits stable ~~decoupling and~~
703 ~~localization~~source location estimation performance with different parameters and remains effective with only a single
704 observation site, as long as the selected site is ~~at an~~appropriately position located. Moreover, the proposed method shows
705 robust source location estimation in the presence of meteorological errors, with mean source location error levels below 10%,
706 on condition that the site layout is appropriate.

707 These results demonstrate that spatiotemporally ~~decoupled-separated~~ source reconstruction is feasible and achieves
708 satisfactory accuracy in the non-constant-release scenarios, thereby providing a promising framework for reconstructing
709 atmospheric radionuclide releases. However, the proposed method does not consider the influence of temporal variations in
710 the release rate on the plume shape. Our future efforts will be directed towards integrating spatial features to further enhance
711 the method.

712
713 *Code and data availability.* The code and data for the proposed method can be downloaded from Zenodo
714 (<https://doi.org/10.5281/zenodo.10200141>). More recent versions of the code and data will be published on GitHub.com
715 (<https://github.com/rocketlab/Source-reconstruction-of-non-constant-atmospheric-radionuclide-releases>, last access: 23
716 November 2023). The implementation is provided in Python, and the instruction file is also available in the provided link.

717

718 *Author contributions.* YX conducted the source reconstruction tests and wrote the manuscript draft; SF provided guidance on
719 the RIMPUFF modeling and suggestions on source reconstruction tests; XD and SZ reviewed and edited the manuscript.

720

721 *Competing interests.* The authors have declared that they have no conflict of interest.

722

723 *Acknowledgements.* This work is supported by the National Natural Science Foundation of China (grant numbers 12275152
724 and 11875037), LingChuang Research Project of China National Nuclear Corporation, and International Atomic Energy
725 Agency (TC project number CRP9053).

726 **References**

- 727 Akhtar, F., Li, J., Pei, Y., Xu, Y., Rajput, A., and Wang, Q.: Optimal Features Subset Selection for Large for Gestational
728 Age Classification Using GridSearch Based Recursive Feature Elimination with Cross-Validation Scheme, in: International
729 Conference on Frontier Computing, 63–71, https://doi.org/10.1007/978-981-15-3250-4_8, 2019.
- 730 Andronopoulos, S. and Kovalets, I. V.: Method of source identification following an accidental release at an unknown
731 location using a lagrangian atmospheric dispersion model, *Atmosphere (Basel)*, 12, 7–12,
732 <https://doi.org/10.3390/atmos12101305>, 2021.
- 733 Anspaugh, L. R., Catlin, R. J., and Goldman, M.: The global impact of the chernobyl reactor accident, *Science (80-.)*, 242,
734 1513–1519, <https://doi.org/10.1126/science.3201240>, 1988.
- 735 Becker, A., Wotawa, G., De Geer, L. E., Seibert, P., Draxler, R. R., Sloan, C., D'Amours, R., Hort, M., Glaab, H., Heinrich,
736 P., Grillon, Y., Shershakov, V., Katayama, K., Zhang, Y., Stewart, P., Hirtl, M., Jean, M., and Chen, P.: Global backtracking
737 of anthropogenic radionuclides by means of a receptor oriented ensemble dispersion modelling system in support of Nuclear-
738 Test-Ban Treaty verification, *Atmos. Environ.*, 41, 4520–4534, <https://doi.org/10.1016/j.atmosenv.2006.12.048>, 2007.
- 739 Chang, J. C. and Hanna, S. R.: Air quality model performance evaluation, *Meteorol. Atmos. Phys.*, 87, 167–196,
740 <https://doi.org/10.1007/s00703-003-0070-7>, 2004.
- 741 Chen, T. and Guestrin, C.: XGBoost: A scalable tree boosting system, *Proc. ACM SIGKDD Int. Conf. Knowl. Discov. Data*
742 *Min.*, 13-17-Aug, 785–794, <https://doi.org/10.1145/2939672.2939785>, 2016.
- 743 Chow, F. K., Kosović, B., and Chan, S.: Source inversion for contaminant plume dispersion in urban environments using
744 building-resolving simulations, *J. Appl. Meteorol. Climatol.*, 47, 1533–1572, <https://doi.org/10.1175/2007JAMC1733.1>,
745 2008.
- 746 Davoine, X. and Bocquet, M.: Inverse modelling-based reconstruction of the Chernobyl source term available for long-range
747 transport, *Atmos. Chem. Phys.*, 7, 1549–1564, <https://doi.org/10.5194/acp-7-1549-2007>, 2007.
- 748 Drews, M., Aage, H. K., Bargholz, K., Ejsing Jørgensen, H., Korsbech, U., Lauritzen, B., Mikkelsen, T., Rojas-Palma, C.,
749 and Ammel, R. Van: Measurements of plume geometry and argon-41 radiation field at the BR1 reactor in Mol, Belgium, 1–

750 43 pp., 2002.

751 Dumont Le Brazidec, J., Bocquet, M., Saunier, O., and Roustan, Y.: MCMC methods applied to the reconstruction of the
752 autumn 2017 Ruthenium-106 atmospheric contamination source, *Atmos. Environ.* X, 6, 100071,
753 <https://doi.org/10.1016/j.aeaoa.2020.100071>, 2020.

754 Dumont Le Brazidec, J., Bocquet, M., Saunier, O., and Roustan, Y.: Quantification of uncertainties in the assessment of an
755 atmospheric release source applied to the autumn 2017 106Ru event, *Atmos. Chem. Phys.*, 21, 13247–13267,
756 <https://doi.org/10.5194/acp-21-13247-2021>, 2021.

757 Eamonn Keogh, Selina Chu, D. H. and M. P.: SEGMENTING TIME SERIES: A SURVEY AND NOVEL APPROACH, in:
758 *Data mining in time series databases*, 1–21, https://doi.org/10.1142/9789812565402_0001, 2004.

759 Efthimiou, G. C., Kovalets, I. V., Venetsanos, A., Andronopoulos, S., Argyropoulos, C. D., and Kakosimos, K.: An
760 optimized inverse modelling method for determining the location and strength of a point source releasing airborne material
761 in urban environment, *Atmos. Environ.*, 170, 118–129, <https://doi.org/10.1016/j.atmosenv.2017.09.034>, 2017.

762 Efthimiou, G. C., Kovalets, I. V., Argyropoulos, C. D., Venetsanos, A., Andronopoulos, S., and Kakosimos, K. E.:
763 Evaluation of an inverse modelling methodology for the prediction of a stationary point pollutant source in complex urban
764 environments, *Build. Environ.*, 143, 107–119, <https://doi.org/10.1016/j.buildenv.2018.07.003>, 2018.

765 Eslinger, P. W. and Schrom, B. T.: Multi-detection events, probability density functions, and reduced location area, *J.*
766 *Radioanal. Nucl. Chem.*, 307, 1599–1605, <https://doi.org/10.1007/s10967-015-4339-3>, 2016.

767 Fang, S., Dong, X., Zhuang, S., Tian, Z., Chai, T., Xu, Y., Zhao, Y., Sheng, L., Ye, X., and Xiong, W.: Oscillation-free
768 source term inversion of atmospheric radionuclide releases with joint model bias corrections and non-smooth competing
769 priors, *J. Hazard. Mater.*, 440, <https://doi.org/10.1016/j.jhazmat.2022.129806>, 2022.

770 Grinsztajn, L., Oyallon, E., and Varoquaux, G.: Why do tree-based models still outperform deep learning on tabular data?,
771 2022.

772 Guo, S., Yang, R., Zhang, H., Weng, W., and Fan, W.: Source identification for unsteady atmospheric dispersion of
773 hazardous materials using Markov Chain Monte Carlo method, *Int. J. Heat Mass Transf.*, 52, 3955–3962,
774 <https://doi.org/10.1016/j.ijheatmasstransfer.2009.03.028>, 2009.

775 Ingremeau, J. and Saunier, O.: Investigations on the source term of the detection of radionuclides in North of Europe in June
776 2020, *EPJ Nucl. Sci. Technol.*, 8, 10, <https://doi.org/10.1051/epjn/2022003>, 2022.

777 Jensen, D. D., Lucas, D. D., Lundquist, K. A., and Glascoe, L. G.: Sensitivity of a Bayesian source-term estimation model to
778 spatiotemporal sensor resolution, *Atmos. Environ.* X, 3, <https://doi.org/10.1016/j.aeaoa.2019.100045>, 2019.

779 Katata, G., Ota, M., Terada, H., Chino, M., and Nagai, H.: Atmospheric discharge and dispersion of radionuclides during the
780 Fukushima Dai-ichi Nuclear Power Plant accident. Part I: Source term estimation and local-scale atmospheric dispersion in
781 early phase of the accident, *J. Environ. Radioact.*, 109, 103–113, <https://doi.org/10.1016/j.jenvrad.2012.02.006>, 2012.

782 Keats, A., Yee, E., and Lien, F. S.: Bayesian inference for source determination with applications to a complex urban
783 environment, *Atmos. Environ.*, 41, 465–479, <https://doi.org/10.1016/j.atmosenv.2006.08.044>, 2007.

784 Keats, A., Yee, E., and Lien, F. S.: Information-driven receptor placement for contaminant source determination, *Environ.*
785 *Model. Softw.*, 25, 1000–1013, <https://doi.org/10.1016/j.envsoft.2010.01.006>, 2010.

786 KIM, J. Y., JANG, H.-K., and LEE, J. K.: Source Reconstruction of Unknown Model Parameters in Atmospheric Dispersion
787 Using Dynamic Bayesian Inference, *Prog. Nucl. Sci. Technol.*, 1, 460–463, <https://doi.org/10.15669/pnst.1.460>, 2011.

788 Kovalets, I. V., Efthimiou, G. C., Andronopoulos, S., Venetsanos, A. G., Argyropoulos, C. D., and Kakosimos, K. E.:
789 Inverse identification of unknown finite-duration air pollutant release from a point source in urban environment, *Atmos.*
790 *Environ.*, 181, 82–96, <https://doi.org/10.1016/j.atmosenv.2018.03.028>, 2018.

791 Kovalets, I. V., Romanenko, O., and Synkevych, R.: Adaptation of the RODOS system for analysis of possible sources of
792 Ru-106 detected in 2017, *J. Environ. Radioact.*, 220–221, <https://doi.org/10.1016/j.jenvrad.2020.106302>, 2020.

793 Li, X., Xiong, W., Hu, X., Sun, S., Li, H., Yang, X., Zhang, Q., Nibart, M., Albergel, A., and Fang, S.: An accurate and
794 ultrafast method for estimating three-dimensional radiological dose rate fields from arbitrary atmospheric radionuclide
795 distributions, *Atmos. Environ.*, 199, 143–154, <https://doi.org/10.1016/j.atmosenv.2018.11.001>, 2019a.

796 Li, X., Sun, S., Hu, X., Huang, H., Li, H., Morino, Y., Wang, S., Yang, X., Shi, J., and Fang, S.: Source inversion of both
797 long- and short-lived radionuclide releases from the Fukushima Daiichi nuclear accident using on-site gamma dose rates, *J.*
798 *Hazard. Mater.*, 379, 120770, <https://doi.org/10.1016/j.jhazmat.2019.120770>, 2019b.

799 Lucas, D. D., Simpson, M., Cameron-Smith, P., and Baskett, R. L.: Bayesian inverse modeling of the atmospheric transport
800 and emissions of a controlled tracer release from a nuclear power plant, *Atmos. Chem. Phys.*, 17, 13521–13543,
801 <https://doi.org/10.5194/acp-17-13521-2017>, 2017.

802 Ma, D., Tan, W., Wang, Q., Zhang, Z., Gao, J., Wang, X., and Xia, F.: Location of contaminant emission source in
803 atmosphere based on optimal correlated matching of concentration distribution, *Process Saf. Environ. Prot.*, 117, 498–510,
804 <https://doi.org/10.1016/j.psep.2018.05.028>, 2018.

805 Masson, O., Steinhauser, G., Zok, D., Saunier, O., Angelov, H., Babić, D., Bečková, V., Bieringer, J., Bruggeman, M.,
806 Burbidge, C. I., Conil, S., Dalheimer, A., De Geer, L. E., De Vismes Ott, A., Eleftheriadis, K., Estier, S., Fischer, H.,
807 Garavaglia, M. G., Gasco Leonarte, C., Gorzkiewicz, K., Hainz, D., Hoffman, I., Hýža, M., Isajenko, K., Karhunen, T.,
808 Kastlander, J., Katzlberger, C., Kierepko, R., Knetsch, G. J., Kövendingé Kónyi, J., Lecomte, M., Mietelski, J. W., Min, P.,
809 Møller, B., Nielsen, S. P., Nikolic, J., Nikolovska, L., Penev, I., Petrinc, B., Povinec, P. P., Querfeld, R., Raimondi, O.,
810 Ransby, D., Ringer, W., Romanenko, O., Rusconi, R., Saey, P. R. J., Samsonov, V., Šilobritiene, B., Simion, E., Söderström,
811 C., Šoštarić, M., Steinkopff, T., Steinmann, P., Sýkora, I., Tabachnyi, L., Todorovic, D., Tomankiewicz, E., Tschiersch, J.,
812 Tsibranski, R., Tzortzis, M., Ungar, K., Vidic, A., Weller, A., Wershofen, H., Zagyvai, P., Zalewska, T., Zapata García, D.,
813 and Zorko, B.: Airborne concentrations and chemical considerations of radioactive ruthenium from an undeclared major
814 nuclear release in 2017, *Proc. Natl. Acad. Sci. U. S. A.*, 116, 16750–16759, <https://doi.org/10.1073/pnas.1907571116>, 2019.

815 Mekhaimr, S. A. and Abdel Wahab, M. M.: Sources of uncertainty in atmospheric dispersion modeling in support of
816 Comprehensive Nuclear–Test–Ban Treaty monitoring and verification system, *Atmos. Pollut. Res.*, 10, 1383–1395,
817 <https://doi.org/10.1016/j.apr.2019.03.008>, 2019.

818 Meutter, P. De and Hoffman, I.: Bayesian source reconstruction of an anomalous Selenium-75 release at a nuclear research
819 institute, *J. Environ. Radioact.*, 218, 106225, <https://doi.org/10.1016/j.jenvrad.2020.106225>, 2020.

820 De Meutter, P., Hoffman, I., and Ungar, K.: On the model uncertainties in Bayesian source reconstruction using an ensemble
821 of weather predictions, the emission inverse modelling system FREAR v1.0, and the Lagrangian transport and dispersion
822 model Flexpart v9.0.2, *Geosci. Model Dev.*, 14, 1237–1252, <https://doi.org/10.5194/gmd-14-1237-2021>, 2021.

823 Monache, L. D., Lundquist, J. K., Kosoví, B., Johannesson, G., Dyer, K. M., Aines, R. D., Chow, F. K., Belles, R. D.,
824 Hanley, W. G., Larsen, S. C., Loosmore, G. A., Nitao, J. J., Sugiyama, G. A., and Vogt, P. J.: Bayesian inference and
825 Markov Chain Monte Carlo sampling to reconstruct a contaminant source on a continental scale, *J. Appl. Meteorol.*
826 *Climatol.*, 47, 2600–2613, <https://doi.org/10.1175/2008JAMC1766.1>, 2008.

827 Nodop, K., Connolly, R., and Girardi, F.: The field campaigns of the European tracer experiment (ETEX): Overview and
828 results, *Atmos. Environ.*, 32, 4095–4108, [https://doi.org/10.1016/S1352-2310\(98\)00190-3](https://doi.org/10.1016/S1352-2310(98)00190-3), 1998.

829 Pisso, I., Sollum, E., Grythe, H., Kristiansen, N. I., Cassiani, M., Eckhardt, S., Arnold, D., Morton, D., Thompson, R. L.,
830 Groot Zwaafink, C. D., Evangeliou, N., Sodemann, H., Haimberger, L., Henne, S., Brunner, D., Burkhardt, J. F., Fouilloux,
831 A., Brioude, J., Philipp, A., Seibert, P., and Stohl, A.: The Lagrangian particle dispersion model FLEXPART version 10.4,
832 *Geosci. Model Dev.*, 12, 4955–4997, <https://doi.org/10.5194/gmd-12-4955-2019>, 2019.

833 Rajaona, H., Septier, F., Armand, P., Delignon, Y., Olry, C., Albergel, A., and Moussafir, J.: An adaptive Bayesian inference
834 algorithm to estimate the parameters of a hazardous atmospheric release, *Atmos. Environ.*, 122, 748–762,
835 <https://doi.org/10.1016/j.atmosenv.2015.10.026>, 2015.

836 Rojas-Palma, C., Aage, H. K., Astrup, P., Bargholz, K., Drews, M., Jørgensen, H. E., Korsbech, U., Lauritzen, B.,
837 Mikkelsen, T., Thykier-Nielsen, S., and Van Ammel, R.: Experimental evaluation of gamma fluence-rate predictions from
838 argon-41 releases to the atmosphere over a nuclear research reactor site, *Radiat. Prot. Dosimetry*, 108, 161–168,
839 <https://doi.org/10.1093/rpd/nch020>, 2004.

840 Saunier, O., Didier, D., Mathieu, A., Masson, O., and Dumont Le Brazidec, J.: Atmospheric modeling and source
841 reconstruction of radioactive ruthenium from an undeclared major release in 2017, *Proc. Natl. Acad. Sci. U. S. A.*, 116,
842 24991–25000, <https://doi.org/10.1073/pnas.1907823116>, 2019.

843 Senocak, I.: Application of a Bayesian inference method to reconstruct short-range atmospheric dispersion events, *AIP Conf.*
844 *Proc.*, 1305, 250–257, <https://doi.org/10.1063/1.3573624>, 2010.

845 Senocak, I., Hengartner, N. W., Short, M. B., and Daniel, W. B.: Stochastic event reconstruction of atmospheric contaminant
846 dispersion using Bayesian inference, *Atmos. Environ.*, 42, 7718–7727, <https://doi.org/10.1016/j.atmosenv.2008.05.024>,
847 2008.

848 Thykier-Nielsen, S., Deme, S., and Mikkelsen, T.: Description of the atmospheric dispersion module RIMPUFF, *Riso Natl.*
849 *Lab. PO Box*, 49, 1999.

850 Tomas, J. M., Peereboom, V., Kloosterman, A., and van Dijk, A.: Detection of radioactivity of unknown origin: Protective
851 actions based on inverse modelling, *J. Environ. Radioact.*, 235–236, 106643, <https://doi.org/10.1016/j.jenvrad.2021.106643>,

852 2021.

853 Ulimoen, M. and Klein, H.: Localisation of atmospheric release of radioisotopes using inverse methods and footprints of
854 receptors as sources, *J. Hazard. Mater.*, 451, <https://doi.org/10.1016/j.jhazmat.2023.131156>, 2023.

855 Wang, Y., Huang, H., Huang, L., and Ristic, B.: Evaluation of Bayesian source estimation methods with Prairie Grass
856 observations and Gaussian plume model: A comparison of likelihood functions and distance measures, *Atmos. Environ.*,
857 152, 519–530, <https://doi.org/10.1016/j.atmosenv.2017.01.014>, 2017.

858 Witte, R. S. and Witte, J. S.: *Statistics*, 496 pp., 2017.

859 Xue, F., Li, X., and Zhang, W.: Bayesian identification of a single tracer source in an urban-like environment using a
860 deterministic approach, *Atmos. Environ.*, 164, 128–138, <https://doi.org/10.1016/j.atmosenv.2017.05.046>, 2017a.

861 Xue, F., Li, X., Ooka, R., Kikumoto, H., and Zhang, W.: Turbulent Schmidt number for source term estimation using
862 Bayesian inference, *Build. Environ.*, 125, 414–422, <https://doi.org/10.1016/j.buildenv.2017.09.012>, 2017b.

863 Yee, E.: Automated computational inference engine for Bayesian source reconstruction: application to some detections/non-
864 detections made in the CTBT international monitoring system, *Appl. Math. Sci.*, 11, 1581–1618,
865 <https://doi.org/10.12988/ams.2017.74149>, 2017.

866 Yee, E., Lien, F. S., Keats, A., and D’Amours, R.: Bayesian inversion of concentration data: Source reconstruction in the
867 adjoint representation of atmospheric diffusion, *J. Wind Eng. Ind. Aerodyn.*, 96, 1805–1816,
868 <https://doi.org/10.1016/j.jweia.2008.02.024>, 2008.

869 Zhao, Y., Liu, Y., Wang, L., Cheng, J., Wang, S., and Li, Q.: Source Reconstruction of Atmospheric Releases by Bayesian
870 Inference and the Backward Atmospheric Dispersion Model: An Application to ETEX-I Data, *Sci. Technol. Nucl. Install.*,
871 2021, <https://doi.org/10.1155/2021/5558825>, 2021.

872 Zhuang, S., Fang, S., Goto, D., Dong, X., Xu, Y., and Sheng, L.: Model behavior regarding in- and below-cloud ¹³⁷Cs wet
873 scavenging following the Fukushima accident using 1-km-resolution meteorological field data, *Sci. Total Environ.*, 872,
874 <https://doi.org/10.1016/j.scitotenv.2023.162165>, 2023.

875